International Journal of Solids and Structures 326 (2026) 113770

Contents lists available at ScienceDirect

International Journal of Solids and Structures

journal homepage: www.elsevier.com/locate/ijsolstr

Numerical analysis of anisotropic plasticity and damage based on the inelastic predictor-elastic corrector method

Zhichao Wei [a,b,*], Sanjeev Koirala [a], Steffen Gerke [a], Michael Brünig [a]

[a] Institute for Engineering Mechanics and Structural Analysis, University of the Bundeswehr Munich, Werner-Heisenberg-Weg 39, D-85577 Neubiberg, Germany
[b] Institute of Metal Forming, RWTH Aachen University, Intzestr. 10, D-52072 Aachen, Germany

ARTICLE INFO

Keywords:
Numerical integration
Numerical analysis
Anisotropic continuum damage model
Biaxial experiments
Finite strains

ABSTRACT

This paper addresses the numerical implementation algorithm for an advanced anisotropic plasticity and damage continuum model. The framework of the proposed theory is based on the introduction of effective undamaged configurations, where no damage occurs, and the damaged configurations that account for elastic–plastic deformation and damage. The anisotropic plastic behavior is characterized by the Hoffman yield condition. The onset of damage is defined by a combination of the first and second deviatoric stress invariants related to the growth and coalescence of micro-defects (micro-voids and micro-shear-cracks). A stress-state-dependent damage strain rate tensor is introduced to capture the damage evolution caused by tension- and shear-induced mechanisms. The constitutive rate equations are numerically integrated using an explicit inelastic (plastic or plastic-damage) predictor-elastic corrector method. The consistent tangent modulus is derived and used to ensure quadratic convergence in the global finite element method. Moreover, numerical calculations for various biaxial loading conditions, including shear- and tension-induced damage mechanisms, demonstrate the accuracy and efficiency of the numerical algorithm. Numerical results are compared with experimental data at both the global load–displacement curve and the local strain fields, measured using the digital image correlation (DIC) technique. Scanning electron microscopy (SEM) is employed to compare the numerically predicted damage mechanism by examining fracture surfaces.

1. Introduction

With technological advancements and the growing demand for resource efficiency, increasing requirements are being placed on materials and structures for economic and lightweight construction. Thus, numerical modeling of the deformation and failure of engineering structures under complex loading conditions is essential, as it enables a detailed understanding of material behavior. For example, anisotropic plasticity significantly influences damage development by inducing different plastic deformations along various loading directions of metal sheets. In addition, load- and displacement-induced damage can reduce material stiffness. Moreover, it is well known that ductile damage and fracture are significantly stress-state dependent (Bai and Wierzbicki, 2008; Brünig et al., 2008; Gao et al., 2010; Mohr and Marcadet, 2015; Wei et al., 2022; Li et al., 2022; Gerke et al., 2024; Zeng and Fang, 2025). Damage initiates and evolves due to the nucleation, growth, and coalescence of micro-voids under tension-dominated stress states, whereas under shear-dominated stress states, it results from the growth and coalescence of micro-shear-cracks. However, accurately measuring damage and quantitatively describing its occurrence and development during experiments remain challenging. Therefore, finite element simulation based on advanced constitutive models has become an important tool for analyzing and predicting the initiation and progression of ductile damage under various loading conditions.

In metal-forming processes such as rolling, extrusion, and deep drawing, anisotropies are induced by internal changes in the crystallographic structure. The Hill yield condition (Hill, 1948), a generalization of the von Mises yield criterion, was proposed to model the anisotropic plastic behavior of ductile metals. In thin sheet metals, the Lankford coefficients are used to characterize anisotropy and can be determined through tensile tests conducted in different directions: RD (rolling direction), DD (diagonal direction), and TD (transverse direction). In addition, Stoughton and Yoon (2009) introduced four hardening curves into the quadratic Hill yield condition, considering the different orientations (RD, DD, and TD) and biaxial tension to characterize the anisotropic hardening behavior. On the other hand, compared to the quadratic Hill yield condition, non-quadratic functions were proposed by Barlat et al. (2005), based on the linear transformation of the stress tensor. These parameters can be identified using uniaxial and biaxial

* Corresponding author at: Institute of Metal Forming, RWTH Aachen University, Intzestr. 10, D-52072 Aachen, Germany.
E-mail address: zhichao.wei@ibf.rwth-aachen.de (Z. Wei).

https://doi.org/10.1016/j.ijsolstr.2025.113770
Received 17 July 2025; Received in revised form 22 October 2025; Accepted 14 November 2025
Available online 14 November 2025
0020-7683/© 2025 The Authors. Published by Elsevier Ltd. This is an open access article under the CC BY-NC-ND license (http://creativecommons.org/licenses/by-nc-nd/4.0/).

tension tests (Barlat et al., 2005; Ha et al., 2018). In addition, Wei et al. (2022) analyzed the tensile and compressive yield stresses for the investigated aluminum alloy and concluded that hydrostatic stress affects the onset of plastic behavior in ductile metals. This phenomenon, known as the stress differential effect, was also observed by Spitzig and Richmond (1984) and Holmen et al. (2017). The Drucker–Prager yield condition (Drucker and Prager, 1952; Brünig, 2001; Wei et al., 2022) is based on incorporating hydrostatic stress into the von Mises yield condition. For anisotropic plasticity, a combination of the first stress invariant and the Hill yield condition (Hoffman, 1967) is used to characterize the anisotropic stress differential (SD) effect, while (Park et al., 2019) incorporates a scaling function into the yield condition proposed by Stoughton and Yoon (2009).

Furthermore, the continuum damage theory is widely used to characterize stiffness degradation in terms of scalar-based (Lemaitre, 1985; Saanouni, 2008; Voyiadjis et al., 2013; Zhang et al., 2025), vector-based (Costin, 1985; Suaris and Shah, 1984), and tensor-based (Voyiadjis and Kattan, 1992; Abu Al-Rub and Voyiadjis, 2003; Brünig, 2003a; Murakami, 2012; Badreddine and Saanouni, 2017; Brünig et al., 2023a) internal variables. Compared to the scalar-based isotropic damage model, the vector- or tensor-based anisotropic damage model can more accurately characterize different degradation behaviors in various loading directions. On the other hand, stress state variables, such as stress triaxiality and the Lode parameter, are effectively utilized in damage and fracture mechanics to differentiate damage mechanisms caused by tension-dominated and shear-dominated states (Brünig et al., 2008; Nahshon and Hutchinson, 2008; Lian et al., 2013; Papasidero et al., 2015; Roth and Mohr, 2016; Wu et al., 2022). For example, (Nahshon and Hutchinson, 2008) introduced the Lode parameter to distinguish shear-dominated damage and fracture in a void-fraction-based GTN model (Tvergaard and Needleman, 1984). Lian et al. (2013) proposed a coupled stress-state-dependent damage and fracture model regarding the damage locus and fracture criteria. Moreover, Brünig et al. (2008) newly introduced stress state variables into the continuum damage framework to describe the anisotropy of damage behavior caused by different loading conditions.

For numerical integration of constitutive rate equations, an explicit plastic predictor-elastic corrector approach was proposed by Nemat-Nasser and Chung (1992) and Nemat-Nasser and Li (1992, 1994) for solving elastic–plastic problems under finite strains. This approach has been extended to address various issues, such as rate-dependent elastoplasticity, elastic-viscoplasticity, and thermal softening effects. The algorithm provides stable and accurate results. Compared to the implicit Euler–backward approach, the explicit Euler method has the advantage of not requiring local iterations. It also demonstrates numerical stability for larger increments, and the above-mentioned plastic predictor–elastic corrector scheme is suitable for ductile metals, which typically undergo large plastic deformations. In addition, Brünig (2001, 2003b) used this approach to address hydrostatic stress-dependent isotropic elastoplasticity and a two-surface anisotropic damage model with isotropic plasticity. It is worth noting that the inelastic (plastic-damage) predictor-elastic corrector method was newly proposed to solve the two-surface elastic–plastic-damage problem (Brünig, 2003b), inspired by Nemat-Nasser and Li (1994). More recently, Wei et al. (2024b) applied it for the numerical integration of two-surface cyclic plasticity and anisotropic damage, considering the combined hardening effect. Although the two-surface plasticity and damage problem may have slightly lower numerical accuracy compared to the widely used implicit approach, it still meets practical engineering requirements. Moreover, certain numerical approaches can be employed to enhance accuracy, such as modifying the estimation of the stress direction (Wang and Atluri, 1994; Nemat-Nasser and Li, 1994) and utilizing numerical integration-related consistent tangent operators (Wei et al., 2024b). A large number of numerical calculations performed under different complex loading conditions confirm that the algorithm provides accurate and stable results for relatively large plastic-damage deformations at global load–displacement curves and local strain fields.

In the present work, compared to the previous isotropic plasticity with an anisotropic damage framework (Brünig, 2003a; Wei et al., 2023), anisotropic plasticity theory is introduced to capture anisotropic plastic behavior. Moreover, the newly proposed formulation of the damage condition and the damage evolution law explicitly accounts for the effect of the rolling direction. This anisotropic damage theory, combined with anisotropic plasticity, extends the previous framework (Brünig, 2003a; Wei et al., 2023) by capturing anisotropic behavior caused by the rolling direction, thereby contributing to more accurate predictions of material behavior where anisotropy plays a significant role. Following the inelastic predictor-elastic corrector integration approach used in Brünig (2003b) and Wei et al. (2024b), the proposed continuum damage model is numerically implemented in the commercial software ANSYS as a user-defined subroutine. In addition, biaxial experiments using cruciform thin X0-specimens, as proposed by Gerke et al. (2017), with different orientations, were conducted to verify the proposed anisotropic damage theory with anisotropic plasticity. The proposed damage model depends on different stress states. Thus, shear loading, one-axial tension, and biaxial loading conditions were designed to study shear-dominated and tension-dominated damage and fracture mechanisms. This paper presents the proposed kinematics and thermodynamics in Section 2 and Section 3, respectively. The proposed anisotropic plasticity and damage constitutive equations are defined in Section 4. Moreover, the numerical integration based on the inelastic predictor-plastic corrector approach and consistent tangent modulus is derived in Section 5. Section 6 describes the flowchart of the proposed algorithm and the numerical setup. The numerical calculations and experimental results, including comparing biaxial experiments from different perspectives, are provided in Section 7. The conclusion is provided in Section 8.

2. Kinematics

The kinematic framework is based on Murakami (1988) and Brünig (2003a), utilizing the effective fictitious undamaged configurations to capture purely elastic–plastic deformations and the damaged configurations to account for elastic–plastic deformed and damaged states. As shown in Fig. 1, in the effective fictitious undamaged configurations, $\mathring{\mathcal{E}}$ is the reference undamaged configuration, while $\overset{*}{\mathcal{E}}$ represents the elastically unloaded and $\mathcal{E}$ describes the current undamaged configuration, respectively. Additionally, $\mathring{\mathcal{B}}$ is reference damaged configuration and $\overset{*}{\mathcal{B}}$ represents the elastically unloaded and $\mathcal{B}$ is the current damaged configuration, respectively. Moreover, the initial damage tensor $\mathring{\mathbf{R}}$ and current damage tensors $\mathbf{R}$ and $\overset{*}{\mathbf{R}}$ are used to map the respective undamaged and damaged configurations.

In the effective fictitious undamaged configurations, the effective metric tensor $\bar{\mathbf{Q}}$ is related to the reference and current effective fictitious undamaged configurations, as shown in Fig. 1. Following the multiplicative decomposition concept for the finite strain Lehmann (1989), Brünig (2001), the effective metric tensor $\bar{\mathbf{Q}}$ is multiplicatively decomposed into an effective plastic part and an elastic part as $\bar{\mathbf{Q}} = \bar{\mathbf{Q}}^{\mathrm{pl}}\bar{\mathbf{Q}}^{\mathrm{el}}$. In addition, the effective logarithmic total strain (Hencky strain) tensor $\bar{\mathbf{A}} = \frac{1}{2}\ln\bar{\mathbf{Q}}$ and elastic strain tensor $\bar{\mathbf{A}}^{\mathrm{el}} = \frac{1}{2}\ln\bar{\mathbf{Q}}^{\mathrm{el}}$ are defined as the logarithms of the effective metric tensor $\bar{\mathbf{Q}}$ and the elastic part of the effective metric tensor $\bar{\mathbf{Q}}^{\mathrm{el}}$, respectively.

Moreover, the rate of the total effective strain tensor is given by

$$\dot{\bar{\mathbf{H}}} = \frac{1}{2}(\ln\bar{\mathbf{Q}})^{\cdot} = \frac{1}{2}\bar{\mathbf{Q}}^{-1}\dot{\bar{\mathbf{Q}}}, \tag{1}$$

and the rate of the effective elastic strain tensor is expressed as

$$\dot{\bar{\mathbf{H}}}^{\mathrm{el}} = \frac{1}{2}(\ln\bar{\mathbf{Q}}^{\mathrm{el}})^{\cdot} = \frac{1}{2}\bar{\mathbf{Q}}^{\mathrm{el}-1}\dot{\bar{\mathbf{Q}}}^{\mathrm{el}}. \tag{2}$$

Considering the multiplicative decomposition of the effective metric tensor, Eq. (1) can be rewritten as

$$\dot{\bar{\mathbf{H}}} = \frac{1}{2}\bar{\mathbf{Q}}^{-1}\dot{\bar{\mathbf{Q}}} = \frac{1}{2}\bar{\mathbf{Q}}^{\mathrm{el}-1}\bar{\mathbf{Q}}^{\mathrm{pl}-1}(\dot{\bar{\mathbf{Q}}}^{\mathrm{pl}}\bar{\mathbf{Q}}^{\mathrm{el}} + \bar{\mathbf{Q}}^{\mathrm{pl}}\dot{\bar{\mathbf{Q}}}^{\mathrm{el}})$$

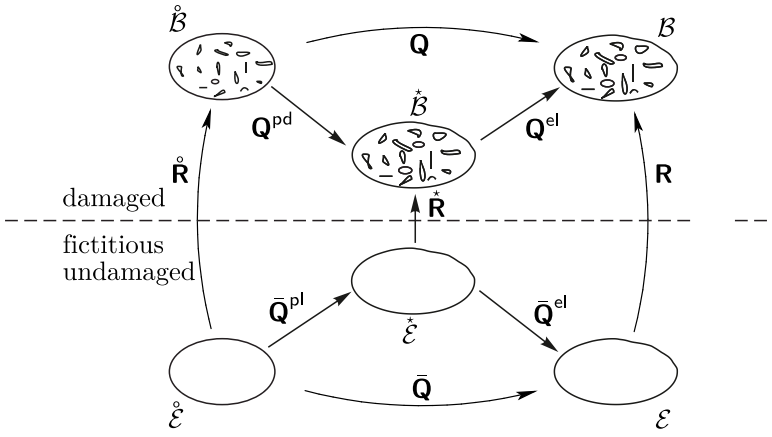

Fig. 1. Configurations and metric transformation tensors.

$$= \frac{1}{2}\bar{\mathbf{Q}}^{\mathrm{el}-1}\bar{\mathbf{Q}}^{\mathrm{pl}-1}\dot{\bar{\mathbf{Q}}}^{\mathrm{pl}}\bar{\mathbf{Q}}^{\mathrm{el}} + \frac{1}{2}\bar{\mathbf{Q}}^{\mathrm{el}-1}\dot{\bar{\mathbf{Q}}}^{\mathrm{el}} = \dot{\bar{\mathbf{H}}}^{\mathrm{pl}} + \dot{\bar{\mathbf{H}}}^{\mathrm{el}}, \tag{3}$$

where the rate of the effective plastic strain tensor is defined as Brünig (2003b)

$$\dot{\bar{\mathbf{H}}}^{\mathrm{pl}} = \frac{1}{2}\bar{\mathbf{Q}}^{\mathrm{el}-1}\bar{\mathbf{Q}}^{\mathrm{pl}-1}\dot{\bar{\mathbf{Q}}}^{\mathrm{pl}}\bar{\mathbf{Q}}^{\mathrm{el}} = \frac{1}{2}\bar{\mathbf{Q}}^{-1}\dot{\bar{\mathbf{Q}}}^{\mathrm{pl}}\bar{\mathbf{Q}}^{\mathrm{el}}. \tag{4}$$

In the damaged configurations, the transformation metric tensor $\mathbf{Q}$ relates the reference and current damaged configurations. It describes the deformation of the damaged material, as also used by Lehmann (1991), and can be computed as $\mathbf{Q} = \mathbf{F}\mathbf{F}^T$, where $\mathbf{F}$ is the deformation gradient tensor. Following the multiplicative decomposition approach for the effective metric transformation tensor $\bar{\mathbf{Q}}$, the same decomposition approach is applied to the metric transformation tensor $\mathbf{Q} = \mathbf{Q}^{\mathrm{pd}}\mathbf{Q}^{\mathrm{el}}$, where $\mathbf{Q}^{\mathrm{pd}}$ and $\mathbf{Q}^{\mathrm{el}}$ are its plastic-damage and elastic parts, respectively. The total and the elastic logarithmic strain tensors (Hencky strain) are calculated as $\mathbf{A} = \frac{1}{2}\ln\mathbf{Q}$ and $\mathbf{A}^{\mathrm{el}} = \frac{1}{2}\ln\mathbf{Q}^{\mathrm{el}}$. In addition, the strain rate tensor is defined in the following form

$$\dot{\mathbf{H}} = \frac{1}{2}\mathbf{Q}^{-1}\dot{\mathbf{Q}} = \frac{1}{2}\mathbf{Q}^{\mathrm{el}-1}\mathbf{Q}^{\mathrm{pd}-1}\dot{\mathbf{Q}}^{\mathrm{pd}}\mathbf{Q}^{\mathrm{el}} + \frac{1}{2}\mathbf{Q}^{\mathrm{el}-1}\dot{\mathbf{Q}}^{\mathrm{el}} = \dot{\mathbf{H}}^{\mathrm{pd}} + \dot{\mathbf{H}}^{\mathrm{el}}, \tag{5}$$

where the elastic and inelastic strain rate tensors are defined as

$$\dot{\mathbf{H}}^{\mathrm{el}} = \frac{1}{2}\mathbf{Q}^{\mathrm{el}-1}\dot{\mathbf{Q}}^{\mathrm{el}}, \tag{6}$$

and

$$\dot{\mathbf{H}}^{\mathrm{pd}} = \frac{1}{2}\mathbf{Q}^{\mathrm{el}-1}\mathbf{Q}^{\mathrm{pd}-1}\dot{\mathbf{Q}}^{\mathrm{pd}}\mathbf{Q}^{\mathrm{el}} = \frac{1}{2}\mathbf{Q}^{-1}\dot{\mathbf{Q}}^{\mathrm{pd}}\mathbf{Q}^{\mathrm{el}}, \tag{7}$$

respectively.

One of the highlights of the proposed kinematic framework is the introduction of the damage strain tensor $\mathbf{A}^{\mathrm{da}}$ in terms of the current damage tensor $\overset{*}{\mathbf{R}}$. As shown in Fig. 1, $\overset{*}{\mathbf{R}}$ describes only the kinematics of the damage deformation. The logarithmic damage strain tensor is given by $\mathbf{A}^{\mathrm{da}} = \frac{1}{2}\ln\overset{*}{\mathbf{R}}$. In addition, the damage strain rate tensor is depicted as $\dot{\mathbf{H}}^{\mathrm{da}} = \frac{1}{2}\overset{*}{\mathbf{R}}^{-1}\dot{\overset{*}{\mathbf{R}}}$. Moreover, based on the kinematic relationships shown in Fig. 1, it can be seen that

$$\mathbf{R} = \bar{\mathbf{Q}}^{\mathrm{el}-1}\mathring{\mathbf{R}}\mathbf{Q}^{\mathrm{el}}, \quad \text{and} \quad \mathbf{Q} = \mathring{\mathbf{R}}^{-1}\bar{\mathbf{Q}}^{\mathrm{pl}}\overset{*}{\mathbf{R}}\mathbf{Q}^{\mathrm{el}}. \tag{8}$$

Thus, substituting Eq. (8) into Eq. (5) and taking into account the formulation of damage strain tensor, one obtains

$$\begin{aligned}
\dot{\mathbf{H}} &= \frac{1}{2}\mathbf{Q}^{-1}\dot{\mathbf{Q}} = \left(\mathbf{Q}^{\mathrm{el}-1}\overset{*}{\mathbf{R}}^{-1}\bar{\mathbf{Q}}^{\mathrm{pl}-1}\mathring{\mathbf{R}}\right)\mathring{\mathbf{R}}^{-1}\left[\dot{\bar{\mathbf{Q}}}^{\mathrm{pl}}\overset{*}{\mathbf{R}}\mathbf{Q}^{\mathrm{el}} + \bar{\mathbf{Q}}^{\mathrm{pl}}\dot{\overset{*}{\mathbf{R}}}\mathbf{Q}^{\mathrm{el}} + \bar{\mathbf{Q}}^{\mathrm{pl}}\overset{*}{\mathbf{R}}\dot{\mathbf{Q}}^{\mathrm{el}}\right] \\
&= \frac{1}{2}\mathbf{Q}^{\mathrm{el}-1}\overset{*}{\mathbf{R}}^{-1}\bar{\mathbf{Q}}^{\mathrm{pl}-1}\dot{\bar{\mathbf{Q}}}^{\mathrm{pl}}\overset{*}{\mathbf{R}}\mathbf{Q}^{\mathrm{el}} + \frac{1}{2}\mathbf{Q}^{\mathrm{el}-1}\overset{*}{\mathbf{R}}^{-1}\dot{\overset{*}{\mathbf{R}}}\mathbf{Q}^{\mathrm{el}} + \frac{1}{2}\mathbf{Q}^{\mathrm{el}-1}\dot{\mathbf{Q}}^{\mathrm{el}} \\
&= \mathbf{R}^{-1}\bar{\mathbf{Q}}^{\mathrm{el}-1}\left(\frac{1}{2}\bar{\mathbf{Q}}^{\mathrm{pl}-1}\dot{\bar{\mathbf{Q}}}^{\mathrm{pl}}\right)\bar{\mathbf{Q}}^{\mathrm{el}}\mathbf{R} + \mathbf{Q}^{\mathrm{el}-1}\left(\frac{1}{2}\overset{*}{\mathbf{R}}^{-1}\dot{\overset{*}{\mathbf{R}}}\right)\mathbf{Q}^{\mathrm{el}} + \frac{1}{2}\mathbf{Q}^{\mathrm{el}-1}\dot{\mathbf{Q}}^{\mathrm{el}} \\
&= \mathbf{R}^{-1}\dot{\bar{\mathbf{H}}}^{\mathrm{pl}}\mathbf{R} + \mathbf{Q}^{\mathrm{el}-1}\dot{\mathbf{H}}^{\mathrm{da}}\mathbf{Q}^{\mathrm{el}} + \dot{\mathbf{H}}^{\mathrm{el}}.
\end{aligned} \tag{9}$$

3. Thermodynamics

The constitutive equations are governed by thermodynamic principles. Consequently, the proposed anisotropic continuum damage model must be thermodynamically consistent. The relationship between energy, stress, and deformation can be established by utilizing the fundamental thermodynamics equations. The constitutive equations for elastic–plastic material behavior are formulated based on the effective fictitious undamaged configurations. Additionally, the constitutive equations for the elastic–plastic-damage behavior of damaged materials are derived considering the damaged configurations.

3.1. Fictitious undamaged configurations

The effective fictitious undamaged configurations characterize elastic–plastic deformations. The rate of the effective specific mechanical work $\dot{w}$ is defined as the scalar product of the effective Kirchhoff stress tensor $\bar{\mathbf{T}}$ and its work conjugate pair the effective strain rate tensor $\dot{\bar{\mathbf{H}}}$

$$\rho_0\dot{w} = \bar{\mathbf{T}}\cdot\dot{\bar{\mathbf{H}}}, \tag{10}$$

where ρ_0 represents the initial mass density. Considering that the rate of effective strain can be additively decomposed into elastic and plastic parts (3). The effective work rate $\dot{w}$ can be further formulated as:

$$\rho_0\dot{w} = \rho_0\dot{w}^{\mathrm{el}} + \rho_0\dot{w}^{\mathrm{pl}} = \bar{\mathbf{T}}\cdot\dot{\bar{\mathbf{H}}}^{\mathrm{el}} + \bar{\mathbf{T}}\cdot\dot{\bar{\mathbf{H}}}^{\mathrm{pl}}. \tag{11}$$

Moreover, the specific effective free Helmholtz energy $\bar{\phi}$ in the effective fictitious undamaged configuration is formulated as the sum of an effective elastic part $\bar{\phi}^{\mathrm{el}}$ and an effective plastic part $\bar{\phi}^{\mathrm{pl}}$, with the hardening effect assumed only to affect the plastic behavior. Following Brünig (2001), it can be written as

$$\bar{\phi} = \bar{\phi}^{\mathrm{el}}(\bar{\mathbf{A}}^{\mathrm{el}}) + \bar{\phi}^{\mathrm{pl}}(\gamma), \tag{12}$$

where γ represents an internal non-negative scalar variable related to strain hardening used to characterize the plastic behavior. Then, the rate of the specific free energy $\dot{\bar{\phi}}$ is obtained as

$$\dot{\bar{\phi}} = \frac{\partial\bar{\phi}^{\mathrm{el}}}{\partial\bar{\mathbf{A}}^{\mathrm{el}}}\cdot\dot{\bar{\mathbf{A}}}^{\mathrm{el}} + \dot{\bar{\phi}}^{\mathrm{pl}}. \tag{13}$$

The Clausius-Duhem inequality, which expresses the second law of thermodynamics, is given by

$$\bar{\mathbf{T}}\cdot\dot{\bar{\mathbf{H}}}^{\mathrm{el}} + \bar{\mathbf{T}}\cdot\dot{\bar{\mathbf{H}}}^{\mathrm{pl}} - \rho_0\frac{\partial\bar{\phi}^{\mathrm{el}}}{\partial\bar{\mathbf{A}}^{\mathrm{el}}}\cdot\dot{\bar{\mathbf{A}}}^{\mathrm{el}} - \rho_0\dot{\bar{\phi}}^{\mathrm{pl}} \geq 0. \tag{14}$$

Moreover, Anand (1979) demonstrated that replacing the infinitesimal strain measure with the Hencky (logarithmic) strain enables the

classical strain–energy function to describe moderately large deformations in good agreement with experiments. Accordingly, following Brünig (1999), the elastic part of the effective free energy is expressed as

$$\rho_0\bar{\phi}^{\mathrm{el}}\left(\bar{\mathbf{A}}^{\mathrm{el}}\right)=G\bar{\mathbf{A}}^{\mathrm{el}}\cdot\bar{\mathbf{A}}^{\mathrm{el}}+\frac{1}{2}\left(K-\frac{2}{3}G\right)\left(\mathrm{tr}\bar{\mathbf{A}}^{\mathrm{el}}\right)^2, \tag{15}$$

and then, using the assumption of $\bar{\mathbf{T}}\cdot\dot{\bar{\mathbf{H}}}^{\mathrm{el}}=\bar{\mathbf{T}}\cdot\dot{\bar{\mathbf{A}}}^{\mathrm{el}}$ proposed by Brünig (2003a), one arrives at the effective Kirchhoff stress tensor

$$\bar{\mathbf{T}}=\rho_0\frac{\partial\bar{\phi}^{\mathrm{el}}}{\partial\bar{\mathbf{A}}^{\mathrm{el}}}=2G\bar{\mathbf{A}}^{\mathrm{el}}+\left(K-\frac{2}{3}G\right)\mathrm{tr}\bar{\mathbf{A}}^{\mathrm{el}}\mathbf{1}, \tag{16}$$

where $\mathbf{1}$ describes the second-order identity tensor, and G represents the shear modulus and K is the bulk modulus.

In addition, the irreversible terms remaining in Eq. (14) form the Kelvin inequality

$$\bar{\mathbf{T}}\cdot\dot{\bar{\mathbf{H}}}^{\mathrm{pl}}-\rho_0\dot{\bar{\phi}}^{\mathrm{pl}}\geq 0 \tag{17}$$

which governs internal dissipation. The effective plastic strain rate tensor characterizes the evolution of the effective plastic deformations.

3.2. Damaged configurations

Considering the elastic–plastic-damage behavior in the damaged configurations, the specific mechanical work $\dot{w}$ is additively split into three parts: an elastic part $\dot{w}^{\mathrm{el}}$, a plastic part $\dot{w}^{\mathrm{pl}}$, and a damage part $\dot{w}^{\mathrm{da}}$. Moreover, with the additive decomposition of the total strain rate $\dot{\mathbf{H}}$ in Eq. (9), the specific mechanical work $\dot{w}$ is rewritten in the form of

$$\rho_0\dot{w}=\rho_0\dot{w}^{\mathrm{el}}+\rho_0\dot{w}^{\mathrm{pl}}+\rho_0\dot{w}^{\mathrm{da}}=\mathbf{T}\cdot\dot{\mathbf{H}}=\mathbf{T}\cdot\dot{\mathbf{H}}^{\mathrm{el}}+\mathbf{R}\mathbf{T}\mathbf{R}^{-1}\cdot\dot{\tilde{\mathbf{H}}}^{\mathrm{pl}}+\tilde{\mathbf{T}}\cdot\dot{\mathbf{H}}^{\mathrm{da}}, \tag{18}$$

where $\tilde{\mathbf{T}}=\mathbf{Q}^{\mathrm{el}}\mathbf{T}\mathbf{Q}^{\mathrm{el}-1}$ is the work conjugate stress tensor of the damage strain rate tensor $\dot{\mathbf{H}}^{\mathrm{da}}$ and $\mathbf{T}$ represents the Kirchhoff stress tensor.

Furthermore, the specific free energy ϕ in the damaged configurations can be decomposed into the elastic ϕ^{el}, plastic ϕ^{pl} and damage ϕ^{da} parts as

$$\phi=\phi^{\mathrm{el}}(\mathbf{A}^{\mathrm{el}},\mathbf{A}^{\mathrm{da}})+\phi^{\mathrm{pl}}(\gamma)+\phi^{\mathrm{da}}(\mu), \tag{19}$$

where μ denotes the equivalent damage strain and damage is considered to degrade the elastic behavior due to the deformation of micro-defects, which leads to the degradation of the elastic properties. Additionally, the plastic flow and damage processes are treated as independent processes, as proposed by Brünig (2003a), Lemaitre (1985), Lu and Chow (1990). Following Hayakawa et al. (1998) and Brünig (2003a), the elastic part of the specific free energy is

$$\begin{aligned}\rho_0\phi^{\mathrm{el}}\left(\mathbf{A}^{\mathrm{el}},\mathbf{A}^{\mathrm{da}}\right)=&\,G\,\mathbf{A}^{\mathrm{el}}\cdot\mathbf{A}^{\mathrm{el}}+\frac{1}{2}\left(K-\frac{2}{3}G\right)\left(\mathrm{tr}\mathbf{A}^{\mathrm{el}}\right)^2+\eta_1\mathrm{tr}\mathbf{A}^{\mathrm{da}}\left(\mathrm{tr}\mathbf{A}^{\mathrm{el}}\right)^2\\&+\eta_2\mathrm{tr}\mathbf{A}^{\mathrm{da}}\mathbf{A}^{\mathrm{el}}\cdot\mathbf{A}^{\mathrm{el}}\\&+\eta_3\mathrm{tr}\mathbf{A}^{\mathrm{el}}\mathbf{A}^{\mathrm{da}}\cdot\mathbf{A}^{\mathrm{el}}+\eta_4\,\mathbf{A}^{\mathrm{el}}\cdot\left(\mathbf{A}^{\mathrm{el}}\mathbf{A}^{\mathrm{da}}\right).\end{aligned} \tag{20}$$

where $\eta_1\ldots\eta_4$ are elastic degradation parameters.

The Clausius–Duham inequality in the damaged configurations is given by

$$\begin{aligned}\rho_0\dot{w}-\rho_0\dot{\phi}=&\mathbf{T}\cdot\dot{\mathbf{H}}^{\mathrm{el}}+\mathbf{R}\mathbf{T}\mathbf{R}^{-1}\cdot\dot{\tilde{\mathbf{H}}}^{\mathrm{pl}}+\tilde{\mathbf{T}}\cdot\dot{\mathbf{H}}^{\mathrm{da}}-\rho_0\frac{\partial\phi^{\mathrm{el}}}{\partial\mathbf{A}^{\mathrm{el}}}\cdot\dot{\mathbf{A}}^{\mathrm{el}}\\&-\rho_0\frac{\partial\phi^{\mathrm{el}}}{\partial\mathbf{A}^{\mathrm{da}}}\cdot\dot{\mathbf{A}}^{\mathrm{da}}-\rho_0\dot{\phi}^{\mathrm{pl}}-\rho_0\dot{\phi}^{\mathrm{da}}\geq 0.\end{aligned} \tag{21}$$

According to Eqs. (20) and (21), the Kirchhoff stress tensor can be calculated as

$$\begin{aligned}\mathbf{T}=\rho_0\frac{\partial\phi^{\mathrm{el}}}{\partial\mathbf{A}^{\mathrm{el}}}=&\,2\left(G+\eta_2\mathrm{tr}\mathbf{A}^{\mathrm{da}}\right)\mathbf{A}^{\mathrm{el}}+\left(K-\frac{2}{3}G+2\eta_1\mathrm{tr}\mathbf{A}^{\mathrm{da}}\right)\mathrm{tr}\mathbf{A}^{\mathrm{el}}\mathbf{1}\\&+\eta_3\left(\mathbf{A}^{\mathrm{da}}\cdot\mathbf{A}^{\mathrm{el}}\right)\mathbf{1}+\eta_3\mathrm{tr}\mathbf{A}^{\mathrm{el}}\mathbf{A}^{\mathrm{da}}\\&+\eta_4\left(\mathbf{A}^{\mathrm{el}}\mathbf{A}^{\mathrm{da}}+\mathbf{A}^{\mathrm{da}}\mathbf{A}^{\mathrm{el}}\right)\end{aligned} \tag{22}$$

with the assumption $\mathbf{T}\cdot\dot{\mathbf{H}}^{\mathrm{el}}=\rho_0\frac{\partial\phi^{\mathrm{el}}}{\partial\mathbf{A}^{\mathrm{el}}}\cdot\dot{\mathbf{A}}^{\mathrm{el}}$ for the reversible elastic term.

Since plasticity and damage are treated as independent processes, the restriction for damage behavior is established as follows:

$$\tilde{\mathbf{T}}\cdot\dot{\mathbf{H}}^{\mathrm{da}}-\rho_0\frac{\partial\phi^{\mathrm{el}}}{\partial\mathbf{A}^{\mathrm{da}}}\cdot\dot{\mathbf{A}}^{\mathrm{da}}-\rho_0\dot{\phi}^{\mathrm{da}}\geq 0. \tag{23}$$

It should be mentioned that the remaining plastic dissipation term in Eq. (21) has already been discussed in the undamaged configurations in Eq. (14).

4. Constitutive equations

This section introduces the anisotropic plastic yield condition f^{pl}, the plastic flow rule, the damage condition f^{da}, and the damage evolution equation. The proposed anisotropic plastic theory assumes that the principal axes of anisotropy align with the principal axes of the stress tensor (Brünig et al., 2023a). The principal axes are aligned as follows: the x-axis corresponds to the rolling direction (RD, 0°), the y-axis lies in the transverse direction (TD, 90°), and in the z-axis is normal to the plane of the sheet. The present work is restricted to discussions under the monotonic loading theory. For anisotropic damage with isotropic plasticity considering the Bauschinger effect under cyclic loading, please refer to Wei et al. (2022, 2023).

4.1. Anisotropic plasticity

Taking the anisotropic plastic behavior and the stress-differential (SD) effect into account, the Hoffman yield condition (Hoffman, 1967) is used

$$f^{\mathrm{pl}}=\mathbf{C}\cdot\bar{\mathbf{T}}+\sqrt{\bar{\mathbf{T}}\cdot\mathbb{D}\bar{\mathbf{T}}}-\bar{c}=a\bar{I}_1^{\mathrm{H}}+\sqrt{2\bar{J}_2^{\mathrm{H}}}-\bar{c}=0, \tag{24}$$

where $\bar{c}$ is the equivalent effective stress, $\bar{\mathbf{T}}$ (16) describes the effective Kirchhoff stress tensor, and $\bar{I}_1^{\mathrm{H}}$ and $\bar{J}_2^{\mathrm{H}}$ are the first effective Hoffman and second effective deviatoric Hoffman invariants, respectively. The definitions of $\bar{I}_1^{\mathrm{H}}$ and $\bar{J}_2^{\mathrm{H}}$ are given by

$$\bar{I}_1^{\mathrm{H}}=\frac{1}{a}\mathbf{C}\cdot\bar{\mathbf{T}}\quad\text{with}\quad a=\frac{1}{3}\mathrm{tr}\mathbf{C}\quad\text{and}\quad\bar{J}_2^{\mathrm{H}}=\frac{1}{2}\bar{\mathbf{T}}\cdot\mathbb{D}\bar{\mathbf{T}}, \tag{25}$$

respectively. In addition, the second-order tensor $\mathbf{C}=C^i_{\cdot j}\,\boldsymbol{g}_i\otimes\boldsymbol{g}^j$ associate with the SD effect in the $x-$, $y-$, and $z-$loading directions, which is given by

$$\left[C^i_{\cdot j}\right]=\begin{bmatrix}C_1&0&0\\0&C_2&0\\0&0&C_3\end{bmatrix}, \tag{26}$$

where C_1, C_2, and C_3 are material constants. These parameters can be calibrated by comparing the tensile and compressive yield stresses in the respective principal loading directions, as proposed by Brünig et al. (2023a).

Moreover, the anisotropic material tensor $\mathbb{D}=D^{i,k}_{\cdot j,l}\,\boldsymbol{g}_i\otimes\boldsymbol{g}^j\otimes\boldsymbol{g}_k\otimes\boldsymbol{g}^l$ is a fourth-order tensor characterizing the anisotropic plasticity, with components

$$\left[D^{i,k}_{\cdot j,l}\right]=\begin{bmatrix}C_4+C_5&-C_4&-C_5&0&0&0\\-C_4&C_4+C_6&-C_6&0&0&0\\-C_5&-C_6&C_5+C_6&0&0&0\\0&0&0&C_7&0&0\\0&0&0&0&C_8&0\\0&0&0&0&0&C_9\end{bmatrix}, \tag{27}$$

where $C_4\ldots C_9$ are material constants related to plastic anisotropy. The discussion of the identified approach for anisotropic parameters $C_4\ldots C_9$ is detailed in Brünig et al. (2021a, 2022, 2023a), in terms of the Lankford coefficients (r-values), which can be calculated based on uniaxial tension and one-axis-loaded tests in different directions. In addition, a short summary of the definition of $C_1\ldots C_9$ is provided in Appendix A. It is noted that the Hoffman yield surface remains conditionally convex (Alzweighi et al., 2022), where the linear stress-differential term $(\mathbf{C}\cdot\bar{\mathbf{T}})$ in the Hoffman criterion (24) does not affect convexity.

The anisotropic material tensor $\mathbb{D}$ is defined as positive semidefinite to ensure convexity, which requires the parameters $C_4 \ldots C_9 \geq 0$.

As reported by many researchers (Spitzig and Richmond, 1984; Brünig, 2003a; Wei et al., 2022), hydrostatic stress has a negligible effect on volume change caused by plastic deformations in iron-based metals. Therefore, the plastic potential function g^{pl} is defined as

$$g^{\mathrm{pl}} = \sqrt{\bar{\mathbf{T}} \cdot \mathbb{D}\bar{\mathbf{T}}} = \sqrt{2\bar{J}_2^{\mathrm{H}}}\,, \tag{28}$$

and the effective plastic strain rate tensor is given by

$$\dot{\bar{\mathbf{H}}}^{\mathrm{pl}} = \dot{\lambda}\frac{\partial g^{\mathrm{pl}}(\sqrt{2\bar{J}_2^{\mathrm{H}}})}{\partial \bar{\mathbf{T}}} = \dot{\lambda}\frac{1}{\sqrt{2\bar{J}_2^{\mathrm{H}}}}\mathbb{D}\bar{\mathbf{T}} = \dot{\lambda}\frac{\|\mathbb{D}\,\bar{\mathbf{T}}\|}{\sqrt{2\bar{J}_2^{\mathrm{H}}}}\frac{\mathbb{D}\bar{\mathbf{T}}}{\|\mathbb{D}\,\bar{\mathbf{T}}\|} = \dot{\gamma}\bar{\mathbf{N}}$$
$$\text{with} \quad \bar{\mathbf{N}} = \frac{\mathbb{D}\bar{\mathbf{T}}}{\|\mathbb{D}\,\bar{\mathbf{T}}\|}\,, \tag{29}$$

where $\dot{\lambda}$ is the non-negative plastic multiplier, $\dot{\gamma}$ represents the rate of the equivalent plastic strain, and $\bar{\mathbf{N}}$ describes the normalized effective deviatoric stress tensor.

In addition, the Voce-type strain hardening is used to characterize isotropic plastic hardening. Thus, the equivalent yield stress is defined as

$$\bar{c} = c_0 + R_0\gamma + R_\infty\left(1 - e^{-b\gamma}\right)\,, \tag{30}$$

where c_0 is the initial yield stress, R_0 and R_∞ are isotropic hardening moduli, b represents the material constant, and γ denotes the equivalent plastic strain.

4.2. Anisotropic damage

Considering damage anisotropy and the stress-state dependence of damage onset, the damage condition is introduced as an additive combination of the first Hoffman stress invariant I_1^{H} and the second deviatoric Hoffman stress invariant $\sqrt{J_2^{\mathrm{H}}}$ (Brünig et al., 2023a)

$$f^{\mathrm{da}} = \alpha\frac{1}{a}\mathbf{C}\cdot\mathbf{T} + \beta\sqrt{\mathbf{T}\cdot\mathbb{D}\mathbf{T}} = \alpha I_1^{\mathrm{H}} + \beta\sqrt{2J_2^{\mathrm{H}}} - \sigma = 0 \quad \text{and} \quad a = \frac{1}{3}\mathrm{tr}\mathbf{C}\,, \tag{31}$$

where α and β are stress-state-dependent parameters, and σ denotes the equivalent damage stress. Moreover, Brünig et al. (2023a) experimentally and numerically analyzed the onset of the damage condition for various stress states considering anisotropic damage. The parameters α and β are given by

$$\alpha\left(\eta^{\mathrm{H}}\right) = \begin{cases} 0 & \text{for } \eta^{\mathrm{H}} \leq 0 \\ \frac{1}{3} & \text{for } \eta^{\mathrm{H}} > 0 \end{cases} \tag{32}$$

and

$$\beta\left(\eta^{\mathrm{H}}, \theta\right) = \begin{cases} 1 & \text{for } \eta^{\mathrm{H}} \leq 0 \\ k(\theta)\,\eta^{\mathrm{H}} + 1 & \text{for } \eta^{\mathrm{H}} > 0 \end{cases}\,, \tag{33}$$

with the generalized Hoffman stress triaxiality

$$\eta^{\mathrm{H}} = \frac{\bar{I}_1^{\mathrm{H}}}{3\sqrt{3\bar{J}_2^{\mathrm{H}}}} \tag{34}$$

and

$$k(\theta) = -0.167\cos^2\theta - 0.062\cos\theta - 1.467\,, \tag{35}$$

respectively, where θ represents the angle with respective the rolling direction.

The damage strain rate tensor is defined as

$$\dot{\mathbf{H}}^{\mathrm{da}} = \dot{\mu}\frac{\partial g^{\mathrm{da}}}{\partial \mathbf{T}} = \dot{\mu}\left(\frac{\tilde{\alpha}}{\sqrt{3}}\mathbf{1} + \tilde{\beta}\mathbf{N}\right) \tag{36}$$

and is derived from the damage potential function

$$g^{\mathrm{da}}\left(I_1, J_2^{\mathrm{H}}\right) = \tilde{\alpha}I_1 + \tilde{\beta}\sqrt{J_2^{\mathrm{H}}}\,, \tag{37}$$

where $\dot{\mu}$ denotes the damage multiplier, $\tilde{\alpha}$ and $\tilde{\beta}$ are stress-state-dependent parameters, and $\mathbf{N} = \frac{\mathbb{D}\mathbf{T}}{\|\mathbb{D}\mathbf{T}\|}$ is the normalized deviatoric stress direction. The damage potential function in (37) ignores the influence of the anisotropic SD effect by using the normal first stress invariant $I_1 = \mathrm{tr}\,\mathbf{T}$ instead of the first Hoffman stress invariant I_1^{H}. This is because negative stress states exhibit shear-dominated damage mechanics, which are accounted for in the second deviatoric terms $\tilde{\beta}\sqrt{J_2^{\mathrm{H}}}$ (37).

Furthermore, the first term ($\dot{\mu}\frac{\tilde{\alpha}}{\sqrt{3}}\mathbf{1}$) of the damage strain rate tensor (36) describes the volume change of the micro-defects under positive stress states, whereas the second deviatoric term characterizes the isochoric deformation of the micro-defects. Experimental and numerical studies on isotropic aluminum alloys under various complex loading conditions (Brünig et al., 2008; Wei et al., 2023, 2024a) confirmed the same concept for formulating the damage strain rate with isotropic plasticity. In addition, Brünig et al. (2023b) conducted a series of micro-simulations to study the volume change and isochoric deformations of micro-defects for anisotropic plasticity under different loading conditions. These simulations derived the generalized stress-state-dependent variables $\tilde{\alpha}$ and $\tilde{\beta}$

$$\tilde{\alpha}\left(\eta^{\mathrm{H}}\right) = \begin{cases} 0.0672\eta^{\mathrm{H}} - 0.2421 & \text{for } \eta^{\mathrm{H}} < 0.21 \\ 2.5161\eta^{\mathrm{H}} - 0.7563 & \text{for } 0.21 \leq \eta^{\mathrm{H}} \leq 0.65 \\ 0.3067\eta^{\mathrm{H}} + 0.6797 & \text{for } \eta^{\mathrm{H}} > 0.65 \end{cases} \tag{38}$$

and

$$\tilde{\beta}\left(\eta^{\mathrm{H}},\, L^{\mathrm{H}}\right) = \begin{cases} 0.9821 & \text{for } \eta^{\mathrm{H}} < 0.45 \\ 1.2442 - 1.2735(\eta^{\mathrm{H}})^2 + 0.0447L^{\mathrm{H}} & \text{for } \eta^{\mathrm{H}} \geq 0.45 \end{cases}\,, \tag{39}$$

where the generalized Hoffman Lode parameter

$$L^{\mathrm{H}} = \frac{-3\sqrt{3}\bar{J}_3^{\mathrm{H}}}{2(\bar{J}_2^{\mathrm{H}})^{3/2}} \quad \text{with} \quad \bar{J}_3^{\mathrm{H}} = \det(\mathbb{D}\bar{\mathbf{T}})\,. \tag{40}$$

Furthermore, the isotropic softening law is chosen to be

$$\sigma = \sigma_0 - H_1\mu^2\,, \tag{41}$$

where σ_0 denotes the initial damage stress, H_1 is the softening modulus, and μ is the equivalent damage strain.

5. Numerical implementation

In this work, an explicit integration approach without iteration is used to solve the internal unknown variables (plastic $\dot{\gamma}$ (29) and damage $\dot{\mu}$ (37) variable), ensuring they satisfy the consistency conditions under the effective fictitious undamaged and damaged configurations. Nemat-Nasser (1991) and Nemat-Nasser and Li (1992) proposed the plastic predictor-elastic corrector method to solve elastic–plastic problems. Brünig (2003b) extended this approach to an inelastic predictor-elastic corrector method for addressing elastic–plastic-damage problems. Recently, Wei et al. (2024b) also used this approach to solve anisotropic damage with isotropic plasticity under cyclic loading conditions.

The numerical integration algorithm aims to compute the incremental quantities for each time step by utilizing the current values of deformations, stresses, and other state variables in conjunction with the constitutive equations. Since the inelastic constitutive relations are expressed in rate form, time discretization is required over the interval $\Delta t = t_{n+1} - t_n$. In this study, all variables are assumed to be known at $t_n = t$.

5.1. Scalar rate equation

5.1.1. Fictitious undamaged configurations

In the effective fictitious undamaged configurations, only elastic–plastic deformations occur. Therefore, only the plastic consistency condition $\dot{f}^{\mathrm{pl}} = 0$ needs to be considered. It is derived from the plastic yield condition (24), one arrives at

$$\dot{\bar{c}} = \frac{\|\mathbb{D}\,\bar{\mathbf{T}}\|}{\sqrt{\bar{\mathbf{T}}\cdot\mathbb{D}\bar{\mathbf{T}}}}\bar{\mathbf{N}}\cdot\dot{\bar{\mathbf{T}}} + \mathbf{C}\cdot\dot{\bar{\mathbf{T}}}\,. \tag{42}$$

In addition, the rate of the effective Kirchhoff stress tensor (16) is given as

$$\dot{\bar{\mathbf{T}}} = 2G\dot{\bar{\mathbf{H}}}^{\mathrm{el}} + \left(K - \frac{2}{3}G\right)\mathrm{tr}\,\dot{\bar{\mathbf{H}}}^{\mathrm{el}}\mathbf{1}\,, \tag{43}$$

and the scalar product

$$\bar{\mathbf{N}}\cdot\dot{\bar{\mathbf{T}}} = 2G\bar{\mathbf{N}}\cdot\dot{\bar{\mathbf{H}}}^{\mathrm{el}}\,, \tag{44}$$

holds since $\bar{\mathbf{N}}$ is a deviatoric tensor, leading to $\bar{\mathbf{N}}\cdot\mathbf{1} = 0$. Furthermore, because plastic deformation does not induce a volume change $\mathrm{tr}\,\dot{\bar{\mathbf{H}}}^{\mathrm{pl}} = 0$. Thus, based on Eq. (5), the trace of the elastic part of the effective strain rate tensor is given by

$$\mathrm{tr}\,\dot{\bar{\mathbf{H}}}^{\mathrm{el}} = \mathrm{tr}(\dot{\bar{\mathbf{H}}} - \dot{\bar{\mathbf{H}}}^{\mathrm{pl}}) = \mathrm{tr}\,\dot{\bar{\mathbf{H}}} \tag{45}$$

Making use of Eqs. (5), (43), (44), and (45), the plastic consistency condition (42) can be written further as

$$\dot{\bar{c}} = \tilde{G}\left(\dot{\varepsilon} - k\dot{\bar{\gamma}}\right) \tag{46}$$

with

$$\dot{\varepsilon} = \left(\frac{2G}{\tilde{G}}\mathbf{C} + \bar{\mathbf{N}}\right)\cdot\dot{\bar{\mathbf{H}}} + \frac{1}{\tilde{G}}\left(K - \frac{2}{3}G\right)\mathrm{tr}\,\dot{\bar{\mathbf{H}}}\,\mathrm{tr}\,\mathbf{C}\,, \tag{47}$$

and

$$\tilde{G} = \frac{\|\mathbb{D}\,\bar{\mathbf{T}}\|}{\sqrt{\bar{\mathbf{T}}\cdot\mathbb{D}\bar{\mathbf{T}}}}G \quad \text{and} \quad k = \frac{2G}{\tilde{G}}\mathbf{C}\cdot\bar{\mathbf{N}} + 1\,. \tag{48}$$

The time integration of the scalar rate Eq. (46) over the time interval Δt is given by

$$\Delta\bar{c} = \tilde{G}\left(\Delta\varepsilon - k\Delta\bar{\gamma}\right). \tag{49}$$

Following the plastic predictor-elastic corrector approach, the total strain increment is initially assumed to be equal to the plastic strain increment, resulting in

$$\Delta\bar{\gamma}_{\mathrm{pr}} = \frac{1}{k}\Delta\varepsilon \tag{50}$$

and the respective predicted equivalent effective stress can be calculated based on Eq. (30)

$$\bar{c}_{\mathrm{pr}} = \bar{c}\left(\bar{\gamma}_{\mathrm{n}} + \Delta\bar{\gamma}_{\mathrm{pr}}\right). \tag{51}$$

It is evident that the predicted equivalent effective plastic strain increment $\Delta\bar{\gamma}$ and equivalent effective stress increment Δc are overestimated due to the neglect of the equivalent elastic strain increment. The error of the equivalent effective plastic strain increment and the equivalent effective stress increment are given by

$$\Delta_{\mathrm{er}}\bar{\gamma} = \Delta\bar{\gamma}_{\mathrm{pr}} - \Delta\bar{\gamma} = \frac{1}{k}\Delta\varepsilon - \Delta\bar{\gamma}\,, \tag{52}$$

and

$$\Delta_{\mathrm{er}}\bar{c} = \bar{c}_{\mathrm{pr}} - \bar{c}_{\mathrm{n+1}} = \bar{c}_{\mathrm{pr}} - \bar{c}_{\mathrm{n}} - \Delta\bar{c}\,. \tag{53}$$

respectively, where $\Delta\bar{c} = \tilde{G}k\Delta_{\mathrm{er}}\bar{\gamma}$, as derived from Eqs. (49) and (52). In addition, the relationship between the error of the equivalent effective plastic strain increment and the error of the equivalent effective stress increment can be expressed as

$$\Delta_{\mathrm{er}}\bar{c} \approx \frac{\partial c}{\partial\bar{\gamma}_{\mathrm{pr}}}\Delta_{\mathrm{er}}\bar{\gamma}. \tag{54}$$

Making use of Eqs. (52), (53), and (54), one gets

$$\Delta_{\mathrm{er}}\bar{\gamma} = \frac{\left(\bar{c}_{\mathrm{pr}} - \bar{c}_{\mathrm{n}}\right)}{\frac{\partial\bar{c}}{\partial\bar{\gamma}_{pr}} + \tilde{G}k}. \tag{55}$$

With the predicted equivalent effective plastic strain increment $\Delta\bar{\gamma}_{\mathrm{pr}}$ (50) and the respective error $\Delta_{\mathrm{er}}\bar{\gamma}$ (55) in hand, the current effective plastic strain increment can be computed in the form of

$$\Delta\bar{\gamma} = \Delta\bar{\gamma}_{\mathrm{pr}} - \Delta_{\mathrm{er}}\bar{\gamma} = \frac{\Delta\varepsilon}{k} - \frac{\bar{c}_{\mathrm{pr}} - \bar{c}_{\mathrm{n}}}{\frac{\partial\bar{c}}{\partial\bar{\gamma}_{pr}} + k\tilde{G}} \tag{56}$$

with

$$\Delta\varepsilon = \left(\frac{2G}{\tilde{G}}\mathbf{C} + \bar{\mathbf{N}}\right)\cdot\Delta\bar{\mathbf{H}} + \frac{1}{\tilde{G}}\left(K - \frac{2}{3}G\right)\mathrm{tr}\,\Delta\bar{\mathbf{H}}\,\mathrm{tr}\,\mathbf{C}\,, \tag{57}$$

and parameter $\tilde{G}$ and k are defined as in Eq. (48).

Therefore, the total current effective plastic strain and the related current effective stress can be calculated using

$$\bar{\gamma}_{\mathrm{n+1}} = \bar{\gamma}_{\mathrm{n}} + \Delta\bar{\gamma} \qquad \text{and} \qquad c_{\mathrm{n+1}} = c_{\mathrm{n}} + \Delta c\,. \tag{58}$$

To calculate the current effective plastic strain increment tensor using the midpoint integration of Eq. (29)

$$\Delta\bar{\mathbf{H}}^{\mathrm{pl}} = \Delta\bar{\gamma}\bar{\mathbf{N}}_{\mathrm{m}} \qquad \text{and} \qquad \bar{\mathbf{N}}_{\mathrm{m}} = \frac{1}{2}\left(\bar{\mathbf{N}}_{\mathrm{n}} + \bar{\mathbf{N}}_{\mathrm{n+1}}\right) \tag{59}$$

with

$$\bar{\mathbf{N}}_{\mathrm{n+1}} = \frac{\mathbb{D}\,\bar{\mathbf{T}}_{\mathrm{n+1}}}{\|\mathbb{D}\,\bar{\mathbf{T}}_{\mathrm{n+1}}\|} \qquad \text{and} \qquad \bar{\mathbf{N}}_{\mathrm{n}} = \frac{\mathbb{D}\,\bar{\mathbf{T}}_{\mathrm{n}}}{\|\mathbb{D}\,\bar{\mathbf{T}}_{\mathrm{n}}\|}\,, \tag{60}$$

the current normalized deviatoric effective stress tensor $\bar{\mathbf{N}}_{\mathrm{n+1}}$ must also be determined. The use of midpoint integration is due to its higher stability compared to the implicit integration method (Ortiz and Popov, 1985). Based on Eq. (60), the change of the normalized deviatoric effective stress tensor can be calculated as

$$\begin{aligned}&\|\mathbb{D}\,\bar{\mathbf{T}}_{\mathrm{n+1}}\|\bar{\mathbf{N}}_{\mathrm{n+1}} - \|\mathbb{D}\,\bar{\mathbf{T}}_{\mathrm{n}}\|\bar{\mathbf{N}}_{\mathrm{n}}\\ &= \mathbb{D}\left(\bar{\mathbf{T}}_{\mathrm{n+1}} - \bar{\mathbf{T}}_{\mathrm{n}}\right)\\ &= \mathbb{D}\left[2G\Delta\bar{\mathbf{H}} - G\Delta\bar{\gamma}\left(\bar{\mathbf{N}}_{\mathrm{n}} + \bar{\mathbf{N}}_{\mathrm{n+1}}\right) + \left(K - \frac{2}{3}G\right)\mathrm{tr}\,\Delta\bar{\mathbf{H}}\mathbf{1}\right].\end{aligned} \tag{61}$$

After some derivations, one arrives at

$$\begin{aligned}\bar{\mathbf{N}}_{\mathrm{n+1}}\|\mathbb{D}\,\bar{\mathbf{T}}_{\mathrm{n+1}}\| = {}& 2G\mathbb{D}\Delta\bar{\mathbf{H}} + \left(K - \frac{2}{3}G\right)\mathrm{tr}\,\Delta\bar{\mathbf{H}}\mathbb{D}\mathbf{1} + \|\mathbb{D}\,\bar{\mathbf{T}}_{\mathrm{n}}\|\bar{\mathbf{N}}_{\mathrm{n}}\\ &- G\Delta\bar{\gamma}\mathbb{D}\left(\bar{\mathbf{N}}_{\mathrm{n}} + \bar{\mathbf{N}}_{\mathrm{n+1}}\right).\end{aligned} \tag{62}$$

Obviously, it is impossible to solve the equation directly since unknown tensor $\bar{\mathbf{N}}_{\mathrm{n+1}}$ appears on both sides of the equation. However, Nemat-Nasser and Li (1992) reported that for elastic–plastic deformation, the final orientation of the stress direction is coaxial with the deviatoric part of the total strain rate tensor

$$\mathbf{N}^{\mathrm{f}} = \frac{\mathrm{dev}\Delta\mathbf{H}}{\|\mathrm{dev}\Delta\mathbf{H}\|}\,. \tag{63}$$

Thus, it is assumed that $\mathbb{D}\bar{\mathbf{N}}_{\mathrm{n+1}} = \mathbb{D}\mathbf{N}^{\mathrm{f}}$, and Eq. (62) can be then written as

$$\bar{\mathbf{N}}_{\mathrm{n+1}} = \frac{2G\mathbb{D}\dot{\bar{\mathbf{H}}} + \left(K - \frac{2}{3}G\right)\mathrm{tr}\,\dot{\bar{\mathbf{H}}}\mathbb{D}\mathbf{1} + \|\mathbb{D}\,\bar{\mathbf{T}}_{\mathrm{n}}\|\bar{\mathbf{N}}_{\mathrm{n}} - G\Delta\bar{\gamma}\mathbb{D}\left(\bar{\mathbf{N}}_{\mathrm{n}} + \mathbf{N}^{\mathrm{f}}\right)}{\|\mathbb{D}\,\bar{\mathbf{T}}_{\mathrm{n+1}}\|}. \tag{64}$$

Now, the current normalized effective deviatoric stress tensor $\bar{\mathbf{N}}_{\mathrm{n+1}}$ (62) can be determined. Consequently, the associated plastic strain increment $\Delta\bar{\mathbf{H}}^{\mathrm{pl}}$ (59) can be calculated. Furthermore, the increment of the elastic strain rate is given as

$$\Delta\mathbf{H}^{\mathrm{el}} = \Delta\mathbf{H} - \Delta\bar{\mathbf{H}}^{\mathrm{pl}}. \tag{65}$$

5.1.2. Damaged configurations

In the damaged configurations, damage occurs with increasing elastic–plastic deformations. Therefore, in addition to the plastic consistency condition (42), the damage consistency condition $\dot{f}^{\mathrm{da}} = 0$ must also be taken into account. As differentiated in Eq. (31), it is given by

$$\dot{\sigma} = \alpha \frac{1}{a}\mathbf{C}\cdot\dot{\mathbf{T}} + \beta \frac{\sqrt{\mathbb{D}\mathbf{T}\cdot\mathbb{D}\mathbf{T}}}{\sqrt{\mathbf{T}\cdot\mathbb{D}\mathbf{T}}}\mathbf{N}\cdot\dot{\mathbf{T}}. \tag{66}$$

The rate of the Kirchhoff stress tensor

$$\begin{aligned}\dot{\mathbf{T}} = {} & 2\left(G+\eta_2 \mathrm{tr}\mathbf{A}^{\mathrm{da}}\right)\dot{\mathbf{H}}^{\mathrm{el}} + \left(K-\frac{2}{3}G+2\eta_1 \operatorname{tr}\mathbf{A}^{\mathrm{da}}\right)\operatorname{tr}\dot{\mathbf{H}}^{\mathrm{el}}\mathbf{1} \\ & + \eta_3\left(\mathbf{A}^{\mathrm{da}}\cdot\dot{\mathbf{H}}^{\mathrm{el}}\right)\mathbf{1} + \eta_3 \operatorname{tr}\dot{\mathbf{H}}^{\mathrm{el}}\mathbf{A}^{\mathrm{da}} \\ & + \eta_4\left(\dot{\mathbf{H}}^{\mathrm{el}}\mathbf{A}^{\mathrm{da}} + \mathbf{A}^{\mathrm{da}}\dot{\mathbf{H}}^{\mathrm{el}}\right) + 2\eta_2 \operatorname{tr}\dot{\mathbf{H}}^{\mathrm{da}}\mathbf{A}^{\mathrm{el}} + 2\eta_1 \operatorname{tr}\dot{\mathbf{H}}^{\mathrm{da}}\operatorname{tr}\mathbf{A}^{\mathrm{el}}\mathbf{1} \\ & + \eta_3\left(\dot{\mathbf{H}}^{\mathrm{da}}\cdot\mathbf{A}^{\mathrm{el}}\right)\mathbf{1} \\ & + \eta_3 \operatorname{tr}\mathbf{A}^{\mathrm{el}}\dot{\mathbf{H}}^{\mathrm{da}} + \eta_4\left(\mathbf{A}^{\mathrm{el}}\dot{\mathbf{H}}^{\mathrm{da}} + \dot{\mathbf{H}}^{\mathrm{da}}\mathbf{A}^{\mathrm{el}}\right).\end{aligned} \tag{67}$$

can be derived from the Kirchhoff stress tensor (22).

Making use of Eq. (9), the elastic strain rate tensor is calculated as

$$\dot{\mathbf{H}}^{\mathrm{el}} = \dot{\mathbf{H}} - \mathbf{R}^{-1}\dot{\mathbf{H}}^{\mathrm{pl}}\mathbf{R} - \mathbf{Q}^{\mathrm{el}-1}\dot{\mathbf{H}}^{\mathrm{da}}\mathbf{Q}^{\mathrm{el}} \tag{68}$$

in the damaged configurations.

Inserting Eqs. (29), (36), (67) , and (68) into Eq. (66), one arrives at

$$\dot{\sigma} = \dot{\varepsilon}_2 - k_3\dot{\gamma} - k_4\dot{\mu} \tag{69}$$

with the scalar coefficients

$$\dot{\varepsilon}_2 = \mathbf{C}_1\cdot\dot{\mathbf{H}}, \tag{70}$$

$$k_3 = \mathbf{R}^{-1}\mathbf{C}_1\mathbf{R}\cdot\dot{\bar{\mathbf{N}}} \tag{71}$$

and

$$k_4 = \left(\mathbf{Q}^{\mathrm{el}-1}\mathbf{C}_1\mathbf{Q}^{\mathrm{el}} - \mathbf{C}_2\right)\cdot\left(\frac{\tilde{\alpha}}{\sqrt{3}}\mathbf{1} + \tilde{\beta}\mathbf{N}\right), \tag{72}$$

where two second-order tensors

$$\begin{aligned}\mathbf{C}_1 = {} & \left[\frac{\alpha}{a}\left(K\operatorname{tr}\mathbf{C} - \frac{2}{3}G\operatorname{tr}\mathbf{C} + 2\operatorname{tr}\mathbf{C}\eta_1\operatorname{tr}\mathbf{A}^{\mathrm{da}} + \eta_3\mathbf{A}^{\mathrm{da}}\cdot\mathbf{C}\right) + \tilde{\beta}\mathbf{N}\cdot\mathbf{A}^{\mathrm{da}}\right]\mathbf{1} \\ & + \frac{\alpha}{a}\left[\left(2G+2\eta_2\mathrm{tr}\mathbf{A}^{\mathrm{da}}\right)\mathbf{C} + \eta_3\operatorname{tr}\mathbf{C}\mathbf{A}^{\mathrm{da}} + 2\eta_4\mathbf{A}^{\mathrm{da}}\operatorname{tr}\mathbf{C}\right] \\ & + \tilde{\beta}\left(2G+2\eta_2\operatorname{tr}\mathbf{A}^{\mathrm{da}}\right)\mathbf{N} + \tilde{\beta}\eta_4\left(\mathbf{N}\mathbf{A}^{\mathrm{da}} + \mathbf{A}^{\mathrm{da}}\mathbf{N}\right)\end{aligned} \tag{73}$$

and

$$\begin{aligned}\mathbf{C}_2 = {} & \left[\frac{\alpha}{a}\left(2\eta_1\operatorname{tr}\mathbf{C}\operatorname{tr}\mathbf{A}^{\mathrm{el}} + 2\eta_2\mathbf{C}\cdot\mathbf{A}^{\mathrm{el}}\right) + 2\tilde{\beta}\eta_2\mathbf{N}\cdot\mathbf{A}^{\mathrm{el}}\right]\mathbf{1} + \tilde{\beta}\eta_3\operatorname{tr}\mathbf{A}^{\mathrm{el}}\mathbf{N} \\ & + \frac{\alpha}{a}\left(\eta_3\operatorname{tr}\mathbf{A}^{\mathrm{el}}\mathbf{C} + 2\eta_4\mathbf{A}^{\mathrm{el}}\mathbf{C} + \eta_3\operatorname{tr}\mathbf{C}\mathbf{A}^{\mathrm{el}}\right) + \tilde{\beta}\eta_4\left(\mathbf{N}\mathbf{A}^{\mathrm{el}} + \mathbf{A}^{\mathrm{el}}\mathbf{N}\right)\end{aligned} \tag{74}$$

has been defined.

As assumed in Murakami (1988) and Brünig (2003a) within homogenization theories, the intermediate configuration corresponds to the current state identically for both undamaged and damaged descriptions (see Fig. 1). Thus, the elastic metric transformation tensors are identical in the undamaged and damaged configurations, $\mathbf{Q}^{\mathrm{el}} = \bar{\mathbf{Q}}^{\mathrm{el}}$, resulting in the effective elastic strain tensor $\dot{\bar{\mathbf{H}}}^{\mathrm{el}}$ being equal to the elastic strain tensor $\dot{\mathbf{H}}^{\mathrm{el}}$ (68), and the plastic consistency condition (42) is updated as

$$\dot{\bar{c}} = \dot{\varepsilon}_1 - k_1\dot{\gamma} - k_2\dot{\mu} \tag{75}$$

with the scalars

$$\dot{\varepsilon}_1 = \mathbf{C}_3\cdot\dot{\mathbf{H}}, \tag{76}$$

$$k_1 = \mathbf{R}^{-1}\mathbf{C}_3\mathbf{R}\cdot\mathbf{N} \tag{77}$$

and

$$k_2 = \mathbf{Q}^{\mathrm{el}-1}\mathbf{C}_3\mathbf{Q}^{\mathrm{el}}\cdot\left(\frac{\tilde{\alpha}}{\sqrt{3}}\mathbf{1} + \tilde{\beta}\mathbf{N}\right), \tag{78}$$

and the tensor

$$\mathbf{C}_3 = \tilde{G}\bar{\mathbf{N}} + 2G\mathbf{C} + \left(K - \frac{2}{3}G\right)\mathbf{1}\operatorname{tr}\mathbf{C}. \tag{79}$$

The integration of the plastic consistency condition (75) and the damage consistency condition (69)

$$\begin{aligned}\Delta\bar{c} &= \Delta\varepsilon_1 - k_1\Delta\gamma - k_2\Delta\mu \\ \Delta\sigma &= \Delta\varepsilon_2 - k_3\Delta\gamma - k_4\Delta\mu.\end{aligned} \tag{80}$$

must both be fulfilled simultaneously, where k_1 (77), k_2 (78), k_3 (71), and k_4 (72) are scalar coefficients. In addition, the equivalent strain increments $\Delta\varepsilon_1$ and $\Delta\varepsilon_2$ are the integration of the equivalent strain rates $\dot{\varepsilon}_1$ (76) and $\dot{\varepsilon}_2$ (70), respectively.

Using the inelastic predictor approach, the equivalent elastic strain increment is assumed to be $\Delta\boldsymbol{\varepsilon}^{\mathrm{el}} = \mathbf{0}$, leading to

$$\begin{bmatrix}k_1 & k_2\\ k_3 & k_4\end{bmatrix}\begin{bmatrix}\Delta\gamma_{\mathrm{pr}}\\ \Delta\mu_{\mathrm{pr}}\end{bmatrix} = \begin{bmatrix}\Delta\varepsilon_1\\ \Delta\varepsilon_2\end{bmatrix} \Longrightarrow \boldsymbol{k}\boldsymbol{f}_{\mathrm{pr}} = \Delta\boldsymbol{e}, \tag{81}$$

where $\boldsymbol{k}$ denotes the coefficient matrix, $\boldsymbol{f}_{\mathrm{pr}}$ is the vector of an inelastic predictor of equivalent strain increments, and $\Delta\boldsymbol{e}$ represents the vector of equivalent strain increments.

The error value of the equivalent effective plastic strain (55) can be derived from Eqs. (52), (53), and (54), and provides the basis for employing the following method to calculate the error vector $\Delta_{\mathrm{er}}\boldsymbol{f}$ as

$$\begin{bmatrix}k_1 + \frac{\partial\bar{c}}{\partial\gamma_{\mathrm{pr}}} & k_2\\ k_3 & k_4 + \frac{\partial\sigma}{\partial\mu_{\mathrm{pr}}}\end{bmatrix}\begin{bmatrix}\Delta_{\mathrm{er}}\gamma\\ \Delta_{\mathrm{er}}\mu\end{bmatrix} = \begin{bmatrix}\bar{c}_{\mathrm{pr}} - \bar{c}_{\mathrm{n}}\\ \sigma_{\mathrm{pr}} - \sigma_{\mathrm{n}}\end{bmatrix} \Longrightarrow \boldsymbol{a}\,\Delta_{\mathrm{er}}\boldsymbol{f} = \Delta\boldsymbol{c}_{\mathrm{pr}} \tag{82}$$

with

$$\bar{c}_{\mathrm{pr}} = \bar{c}\left(\gamma_{\mathrm{n}} + \Delta\gamma_{\mathrm{pr}}\right) \quad \text{and} \quad \sigma_{\mathrm{pr}} = \sigma\left(\mu_{\mathrm{n}} + \Delta\mu_{\mathrm{pr}}\right). \tag{83}$$

Solving the given system of Eqs. (81) and (82), the increments of equivalent strains are given by

$$\begin{aligned}\Delta\boldsymbol{f} &= \Delta\boldsymbol{f}_{\mathrm{pr}} - \Delta\boldsymbol{f}_{\mathrm{er}} = \boldsymbol{k}^{-1}\Delta\boldsymbol{e} - \boldsymbol{a}^{-1}\Delta\boldsymbol{c}_{\mathrm{pr}} \\ \begin{bmatrix}\Delta\gamma\\ \Delta\mu\end{bmatrix} &= \begin{bmatrix}k_1 & k_2\\ k_3 & k_4\end{bmatrix}^{-1}\begin{bmatrix}\Delta\varepsilon_1\\ \Delta\varepsilon_2\end{bmatrix} - \begin{bmatrix}k_1 + \frac{\partial\bar{c}}{\partial\gamma_{\mathrm{pr}}} & k_2\\ k_3 & k_4 + \frac{\partial\sigma}{\partial\mu_{\mathrm{pr}}}\end{bmatrix}^{-1}\begin{bmatrix}\bar{c}_{\mathrm{pr}} - \bar{c}_{\mathrm{n}}\\ \sigma_{\mathrm{pr}} - \sigma_{\mathrm{n}}\end{bmatrix}.\end{aligned} \tag{84}$$

Analogous to the effective plastic strain increment tensor $\Delta\bar{\mathbf{H}}^{\mathrm{pl}}$ (59), which is integrated using the midpoint approach, the current damage strain increment can be computed in the following form

$$\Delta\mathbf{H}^{\mathrm{da}} = \Delta\mu\left(\frac{\tilde{\alpha}}{\sqrt{3}}\mathbf{1} + \tilde{\beta}\mathbf{N}_{\mathrm{m}}\right) \quad \text{and} \quad \mathbf{N}_{\mathrm{m}} = \frac{1}{2}\left(\mathbf{N}_{\mathrm{n}} + \mathbf{N}_{\mathrm{n+1}}\right) \tag{85}$$

with

$$\mathbf{N}_{\mathrm{n+1}} = \frac{\mathbb{D}\,\mathbf{T}_{\mathrm{n+1}}}{\left\|\mathbb{D}\,\mathbf{T}_{\mathrm{n+1}}\right\|} \quad \text{and} \quad \mathbf{N}_{\mathrm{n}} = \frac{\mathbb{D}\,\mathbf{T}_{\mathrm{n}}}{\left\|\mathbb{D}\,\mathbf{T}_{\mathrm{n}}\right\|}, \tag{86}$$

Making use of Eqs. (59), (85), and (86), the change in the normalized deviatoric stress tensor can be calculated as

$$\begin{aligned}&\left\|\mathbb{D}\,\mathbf{T}_{\mathrm{n+1}}\right\|\mathbf{N}_{\mathrm{n+1}} - \left\|\mathbb{D}\,\mathbf{T}_{\mathrm{n}}\right\|\mathbf{N}_{\mathrm{n}} \\ &= \mathbb{D}\left(\mathbf{T}_{\mathrm{n+1}} - \mathbf{T}_{\mathrm{n}}\right) \\ &= 2G\mathbb{D}\Delta\bar{\mathbf{H}} - \Delta\gamma G\mathbb{D}(\bar{\mathbf{N}}_{\mathrm{n}} + \bar{\mathbf{N}}_{\mathrm{n+1}}) \\ &- 2\Delta\mu G\mathbb{D}\left(\frac{\tilde{\alpha}}{\sqrt{3}}\mathbf{1} + \frac{\tilde{\beta}}{2}\left(\mathbf{N}_{\mathrm{n}} + \mathbf{N}_{\mathrm{n+1}}\right)\right) + \left(K - \frac{2}{3}G\right)\operatorname{tr}\Delta\bar{\mathbf{H}}\mathbb{D}\mathbf{1}.\end{aligned} \tag{87}$$

It can be observed that the current effective normalized deviatoric stress tensor $\bar{\mathbf{N}}_{\mathrm{n+1}}$ and the normalized deviatoric stress tensor $\mathbf{N}_{\mathrm{n+1}}$ are unknown and appear on both sides of the equation, making it impossible to be solved directly. Therefore, two main assumptions are introduced. First, Wei et al. (2024b) analyzed a series of numerical results and indicated that assuming the current effective normalized deviatoric stress tensor $\bar{\mathbf{N}}_{\mathrm{n+1}}$ remains unchanged leads to better convergence behavior compared to keeping the normalized deviatoric stress tensor $\mathbf{N}_{\mathrm{n+1}}$ constant. Consequently, the change in the effective normalized deviatoric stress is considered negligible, i.e., $\bar{\mathbf{N}}_{\mathrm{n+1}} = \bar{\mathbf{N}}_{\mathrm{n}} = \bar{\mathbf{N}}_{\mathrm{m}}$. Second, a similar assumption is applied as in the effective fictitious

undamaged configuration, i.e., $\mathbb{D}\mathbf{N}_{n+1} \approx \mathbb{D}\bar{\mathbf{N}}^{f}$. Hence, the current normalized deviatoric stress tensor can be calculated as

$$\mathbf{N}_{n+1} = \frac{\mathbb{D}\left(\Delta\mathbf{H} - \Delta\gamma\bar{\mathbf{N}}_n\right) + \frac{K-\frac{2}{3}G}{2G}\,\mathrm{tr}\,\Delta\bar{\mathbf{H}}\mathbb{D}\mathbf{1} + \frac{\|\mathbb{D}\mathbf{T}_n\|}{2G}\mathbf{N}_n - G\Delta\mu\mathbb{D}\left(\frac{\tilde{\alpha}}{\sqrt{3}}\mathbf{1} + \frac{\tilde{\beta}}{2}\bar{\mathbf{N}}^{f} + \frac{\tilde{\beta}}{2}\mathbf{N}_n\right)}{\|\mathbb{D}\,\mathbf{T}_{n+1}\|}. \tag{88}$$

It is worth noting that the assumption of constant effective normalized deviatoric stress may cause numerical issues under extreme non-proportional loading conditions, particularly when loading direction changes occur during damage evolution. This can be addressed by adjusting the time step size. For most non-proportional loading cases, however, changes in loading direction initially result in elastic–plastic behavior without damage evolution, and damage develops only during subsequent loading. Therefore, the assumption has no significant influence, as confirmed by numerical studies performed by Wei et al. (2025b).

Consequently, the current plastic strain increment tensor $\Delta\bar{\mathbf{H}}^{pl}$(59) and the current damage strain increment $\Delta\mathbf{H}^{da}$(85) can be calculated. Then, the current damage tensor $\overset{*}{\mathbf{R}}$ can be computed as

$$\overset{*}{\mathbf{R}} = \overset{*}{\mathbf{R}}_{n-1}\left(\mathbf{1} - \Delta\mathbf{H}^{da}\right)^{-1}\left(\mathbf{1} + \Delta\mathbf{H}^{da}\right). \tag{89}$$

In addition, the elastic Hencky strain increment $\Delta\mathbf{H}^{el}$ is determined by integrating the elastic strain rate tensor $\dot{\mathbf{H}}^{el}$ (68) as

$$\Delta\mathbf{H}^{el} = \Delta\mathbf{H} - \mathbf{R}^{-1}\Delta\bar{\mathbf{H}}^{pl}\mathbf{R} - \mathbf{Q}^{el-1}\Delta\mathbf{H}^{da}\mathbf{Q}^{el}. \tag{90}$$

5.2. Consistent tangent moduli

To achieve quadratic convergence in the global finite element method, consistent tangent moduli are needed, and the Newton–Raphson scheme is utilized to efficiently solve the incremental problem. In addition, the current effective Kirchhoff stress $\bar{\mathbf{T}}$ is calculated based on Hooke's law in Eq. (16), whereas the current Kirchhoff stress $\mathbf{T}$ is determined by Eq. (22). Furthermore, all tangent moduli are based on the current Kirchhoff stress. However, if no previous damage occurs, the current effective stress $\bar{\mathbf{T}}$ equals the current stress $\mathbf{T}$, simplifying the calculation of the tangent modulus. Thus, various formulations of consistent tangent moduli will be presented in this subsection.

5.2.1. Elastic tangent modulus

Based on Eq. (22), the elastic-damage tangent modulus can be calculated as

$$\begin{aligned}\mathbb{C}^{el,d} &= \frac{\mathrm{d}\mathbf{T}}{\mathrm{d}\mathbf{A}^{el}}\\ &= 2(G + \eta_2\mathrm{tr}\mathbf{A}_n^{da})\mathbb{1} + (K - \frac{2}{3}G + 2\eta_1\mathrm{tr}\mathbf{A}_n^{da})\mathbf{1}\otimes\mathbf{1}\\ &\quad + \eta_3(\mathbf{A}_n^{da}\otimes\mathbf{1} + \mathbf{1}\otimes\mathbf{A}_n^{da}) + \eta_4\mathbb{A}_n^{da}\end{aligned} \tag{91}$$

with

$$\mathbb{1} = \frac{1}{2}(\delta_k^i\delta_j^l + \delta^{il}\delta_{jk})\mathbf{g}_i\otimes\mathbf{g}^k\otimes\mathbf{g}_l\otimes\mathbf{g}^j \quad\text{and}\quad \mathbb{A}_n^{da} = (\mathbf{A}_n^{da})_l^i\delta_j^k + (\mathbf{A}_n^{da})_k^j\delta_l^i, \tag{92}$$

where $\mathbf{A}_n^{da}$ is the historical damage strain tensor. In addition, if no previous damage occurs, $\mathbf{A}_n^{da} = \mathbf{0}$ and $\mu_n = 0$, the current effective Kirchhoff stress equals the current Kirchhoff stress, and the elastic tangent can be simplified as

$$\mathbb{C}^{el} = \mathbb{C}^{el,d}(\mathbf{A}_n^{da} = \mathbf{0}) = \frac{\mathrm{d}\bar{\mathbf{T}}}{\mathrm{d}\mathbf{A}^{el}} = 2G\mathbb{1} + (K - \frac{2}{3}G)\mathbf{1}\otimes\mathbf{1}. \tag{93}$$

5.2.2. Elastic–plastic tangent modulus

According to Eqs. (3) and (91), the stress differential is given by

$$\mathrm{d}\mathbf{T} = \frac{\mathrm{d}\mathbf{T}}{\mathrm{d}\mathbf{A}^{el}}\mathbf{A}^{el} = \mathbb{C}^{el,d}\mathrm{d}\mathbf{A}^{el}, \tag{94}$$

and the elastic strain differential can be computed in the undamaged configurations

$$\mathrm{d}\mathbf{A}^{el} = \mathrm{d}\bar{\mathbf{H}}^{el} = \mathrm{d}\bar{\mathbf{H}} - \mathrm{d}\bar{\mathbf{H}}^{pl} = \mathrm{d}\bar{\mathbf{H}} - \mathrm{d}\bar{\gamma}\bar{\mathbf{N}}_m. \tag{95}$$

Furthermore, with the plastic consistency condition Eq. (46) and the plastic constitutive law

$$\mathrm{d}\bar{c} = \frac{\partial\bar{c}}{\partial\bar{\gamma}}\mathrm{d}\gamma = \tilde{G}(\Delta\varepsilon - k\Delta\bar{\gamma}). \tag{96}$$

Making use of Eqs. (56) and (96)

$$\mathrm{d}\bar{\gamma} = \frac{\tilde{G}\left[\left(\frac{2G}{\tilde{G}}\mathbf{C} + \bar{\mathbf{N}}\right)\cdot\mathrm{d}\bar{\mathbf{H}} + \frac{K-\frac{2}{3}G}{\tilde{G}}\,\mathrm{tr}\,\mathrm{d}\bar{\mathbf{H}}\,\mathrm{tr}\,\mathbf{C}\right]}{\frac{\partial\bar{c}}{\partial\bar{\gamma}} + \tilde{G}k}, \tag{97}$$

the differential of the elastic rate tensor can be written as

$$\begin{aligned}\mathrm{d}\bar{\mathbf{H}}^{el} &= \mathrm{d}\bar{\mathbf{H}} - \mathrm{d}\bar{\gamma}\bar{\mathbf{N}}_m\\ &= \left[\mathbf{1}\otimes\mathbf{1} - \frac{\tilde{G}\bar{\mathbf{N}}_m\otimes\bar{\mathbf{N}} + 2G\bar{\mathbf{N}}_m\otimes\mathbf{C}}{\frac{\partial\bar{c}}{\partial\bar{\gamma}} + \tilde{G}k} - \frac{\left(K - \frac{2}{3}G\right)\mathrm{tr}\,\mathbf{C}}{\frac{\partial\bar{c}}{\partial\bar{\gamma}} + \tilde{G}k}\bar{\mathbf{N}}_m\otimes\mathbf{1}\right]\mathrm{d}\bar{\mathbf{H}}.\end{aligned} \tag{98}$$

Substituting Eq. (95) into Eq. (94), the elastic–plastic tangent modulus with previous damage is

$$\mathbb{C}^{ep,d} = \mathbb{C}^{el,d} - \frac{2G\left(\tilde{G}\bar{\mathbf{N}}_m\otimes\bar{\mathbf{N}} + 2G\bar{\mathbf{N}}_m\otimes\mathbf{C}\right) + 2G\left(K - \frac{2}{3}G\right)\mathrm{tr}\,\mathbf{C}\,\bar{\mathbf{N}}_m\otimes\mathbf{1}}{\frac{\partial\bar{c}}{\partial\bar{\gamma}} + \tilde{G}k}. \tag{99}$$

Again, if there is no previous damage, $\mathbf{A}_n^{da} = \mathbf{0}$ and $\mu_n = 0$, the elastic–plastic tangent can be simplified as

$$\mathbb{C}^{ep} = \mathbb{C}^{el} - \frac{2G\left(\tilde{G}\bar{\mathbf{N}}_m\otimes\bar{\mathbf{N}} + 2G\bar{\mathbf{N}}_m\otimes\mathbf{C}\right) + 2G\left(K - \frac{2}{3}G\right)\mathrm{tr}\,\mathbf{C}\,\bar{\mathbf{N}}_m\otimes\mathbf{1}}{\frac{\partial\bar{c}}{\partial\bar{\gamma}} + \tilde{G}k}. \tag{100}$$

5.2.3. Elastic–plastic-damage modulus

Based on Eq. (22), the stress differential in the damage configurations is given by

$$\mathrm{d}\mathbf{T} = \mathbb{C}^{epd}\mathrm{d}\mathbf{H} = \mathbb{C}^{el,d}\mathrm{d}\mathbf{A}^{el} + \mathbb{C}^{da}\mathrm{d}\mathbf{A}^{da} = \frac{\mathrm{d}\mathbf{T}}{\mathrm{d}\mathbf{A}^{el}}\mathrm{d}\mathbf{A}^{el} + \frac{\mathrm{d}\mathbf{T}}{\mathrm{d}\mathbf{A}^{da}}\mathrm{d}\mathbf{A}^{da} \tag{101}$$

with

$$\mathbb{C}^{da} = \frac{\mathrm{d}\mathbf{T}}{\mathrm{d}\mathbf{A}^{da}} = 2\eta_1\mathrm{tr}\mathbf{A}^{el}\mathbf{1}\otimes\mathbf{1} + 2\eta_2\mathbf{A}^{el}\otimes\mathbf{1} + \eta_3\mathbf{1}\otimes\mathbf{A}^{el} + \eta_3\mathrm{tr}\mathbf{A}^{el}\mathbb{1} + \eta_4\mathbb{A}^{el} \tag{102}$$

and

$$\mathbb{A}^{el} = (\mathbf{A}^{el})_{.k}^{i}\delta_{.j}^{l} + \delta_{.k}^{i}(\mathbf{A}^{el})_{.j}^{l}. \tag{103}$$

In addition, the elastic strain differential is given by, see Eq. (68),

$$\mathrm{d}\mathbf{A}^{el} = \mathrm{d}\mathbf{H}^{el} = \mathrm{d}\mathbf{H} - \mathrm{d}\gamma\mathbf{R}^{-1}\bar{\mathbf{N}}_m\mathbf{R} - \mathrm{d}\mu\mathbf{Q}^{el-1}(\tilde{\alpha}\frac{1}{\sqrt{3}}\mathbf{1} + \tilde{\beta}\tilde{\mathbf{N}}_m)\mathbf{Q}^{el}. \tag{104}$$

Making use of Eqs. (81) and (82), one gets

$$\mathrm{d}\boldsymbol{f}_{er} = \boldsymbol{a}^{-1}\mathrm{d}\boldsymbol{c}_{pr} = \boldsymbol{a}^{-1}\boldsymbol{h}\,\mathrm{d}\boldsymbol{f}_{pr} \quad\text{with}\quad \boldsymbol{h} = \begin{bmatrix}\frac{\partial\bar{c}}{\partial\gamma} & 0\\ 0 & \frac{\partial\sigma}{\partial\mu}\end{bmatrix}, \tag{105}$$

and

$$\mathrm{d}\boldsymbol{f}_{pr} = \boldsymbol{k}^{-1}\mathrm{d}\boldsymbol{e}. \tag{106}$$

Subtracting Eq. (105) from Eq. (106), one arrives at

$$\begin{aligned}&\mathrm{d}\boldsymbol{f} = \mathrm{d}\boldsymbol{f}_{pr} - \mathrm{d}\boldsymbol{f}_{er} = \left(\boldsymbol{k}^{-1} - \boldsymbol{a}^{-1}\boldsymbol{h}\,\boldsymbol{k}^{-1}\right)\mathrm{d}\boldsymbol{e} = \boldsymbol{b}\mathrm{d}\boldsymbol{e}\\ &\Longrightarrow \begin{bmatrix}\mathrm{d}\gamma\\ \mathrm{d}\mu\end{bmatrix} = \begin{bmatrix}b_{11} & b_{12}\\ b_{21} & b_{22}\end{bmatrix}\begin{bmatrix}\mathbf{C}_3\cdot\mathrm{d}\mathbf{H}\\ \mathbf{C}_1\cdot\mathrm{d}\mathbf{H}\end{bmatrix}.\end{aligned} \tag{107}$$

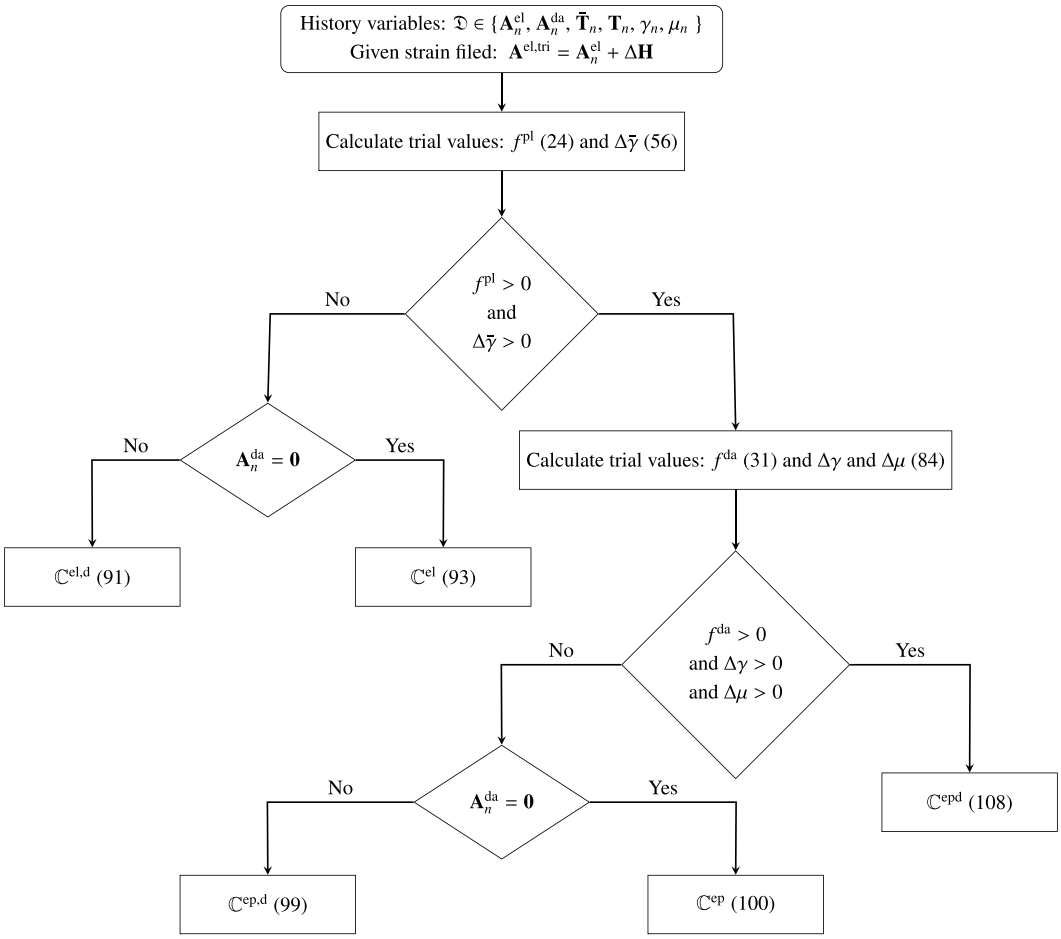

Fig. 2. Flowchart for the proposed algorithm based on the inelastic predictor-elastic corrector approach.

Making use of Eqs. (101), (104), and (107), the elastic–plastic-damage tangent modulus $\mathbb{C}^{\mathrm{epd}}$ is given by

$$\begin{aligned}\mathbb{C}^{\mathrm{epd}} = \mathbb{C}^{\mathrm{el}} &- \mathbb{C}^{\mathrm{el}}\left(\mathbf{R}^{-1}\bar{\mathbf{N}}_{\mathrm{m}}\mathbf{R}\right) \otimes \left(b_{11}\mathbf{C}_3 + b_{12}\mathbf{C}_1\right) \\ &- \mathbb{C}^{\mathrm{el}}\left(\frac{\tilde{\alpha}}{\sqrt{3}}\mathbf{1} + \tilde{\beta}\mathbf{Q}^{\mathrm{el}-1}\mathbf{N}_{\mathrm{m}}\mathbf{Q}^{\mathrm{el}}\right) \otimes \left(b_{21}\mathbf{C}_3 + b_{22}\mathbf{C}_1\right) \\ &+ \mathbb{C}^{\mathrm{da}}\left(\frac{\tilde{\alpha}}{\sqrt{3}}\mathbf{1} + \tilde{\beta}\mathbf{N}_{\mathrm{m}}\right) \otimes \left(b_{21}\mathbf{C}_3 + b_{22}\mathbf{C}_1\right)\end{aligned} \tag{108}$$

6. Numerical setups

This paper focuses on discussing the numerical simulations with the proposed material model. Hence, the experimental data for biaxially loaded X0-specimens are taken from previous publications (Brünig et al., 2021a), where the Hill48 model from the commercial software ANSYS was used. The experimental setups and procedures are also presented in Brünig et al. (2021a). This section describes the numerical aspects of the algorithm implementation environment, boundary conditions, and a brief introduction to the material properties and their parameters.

6.1. Algorithm

In this work, the proposed material model is implemented as a user-defined subroutine in the commercial software ANSYS APDL. The default global force convergence is 10^{-3}. Moreover, using the explicit numerical integration method with an inelastic predictor–elastic corrector approach to integrate the constitutive rate equations results in effective computational performance. Moreover, a larger number of numerical simulations using the aforementioned inelastic predictor–elastic corrector method have shown stable and higher accuracy compared to a wide range of experiments under different complex conditions (Wei et al., 2022, 2023, 2024b). In this work, a novel anisotropic damage and anisotropic plasticity model is proposed to more accurately characterize anisotropic material behavior.

The implementation algorithm is presented in Fig. 2. The plastic condition f^{pl} (24) is first checked, and the equivalent plastic strain increment $\Delta\bar{\gamma}$ (56) is calculated. If the $f^{\mathrm{pl}} \leq 0$ or $\Delta\bar{\gamma} \leq 0$, the elastic routine is activated; otherwise, the damage condition f^{da} (31) is checked, and the corresponding equivalent plastic strain and damage strain increments $\Delta\gamma$ and $\Delta\mu$ (84) are computed. If the f^{da}, $\Delta\gamma$, or $\Delta\mu$ is less than zero, the plastic routine is activated; otherwise, the plastic-damage routine is activated. The active set strategy (Simo and Hughes, 1998) improves efficiency and accuracy by applying the respective constraints under different loading conditions between the effective undamaged and damaged configurations.

6.2. Boundary conditions and meshes

The geometry of the X0-specimen and corresponding mesh is shown in Fig. 3. It has a fourfold symmetric geometry along axes 1, 2, and the diagonal directions, ensuring identical stress states regardless of whether the load is applied along axis 1 or axis 2, respectively. The design of the center notch localizes strain and stress in the notch area, resulting in failure occurring in this region. In addition, applying positive and negative loads along axes 1 and 2 induces a near-zero stress state. It has been confirmed that different loading combination ratios $\xi = F_1 : F_2$ (Fig. 3(b)) generate various stress states, enabling the

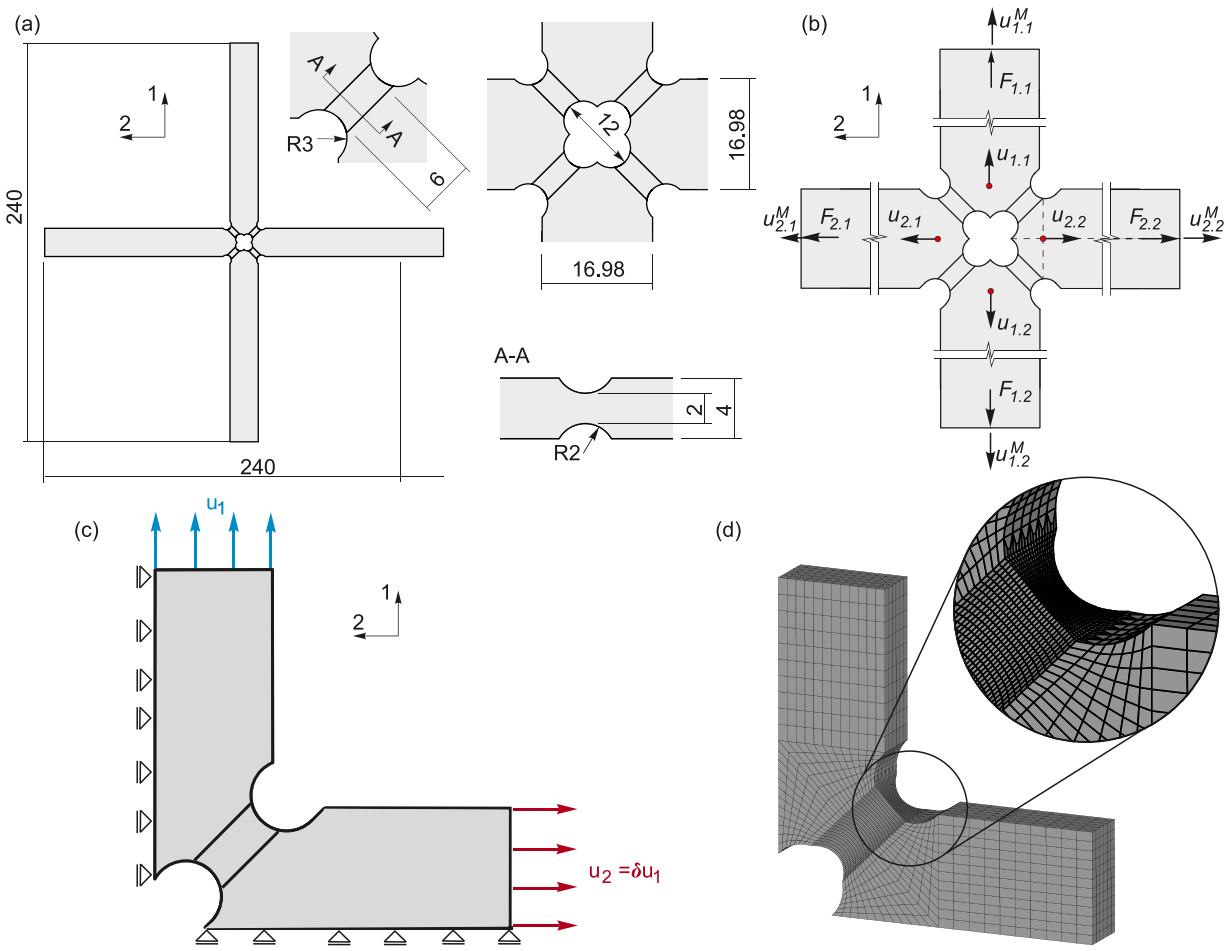

Fig. 3. Geometry and mesh:(a) sketch of the X0-specimen and details of the notch part (all dimensions in mm), (b) measure points for experiments and numerical calculations, (c) displacement boundary conditions, and (d) mesh of the X0-specimen.

investigation of different damage mechanisms under different loading conditions (Brünig et al., 2021a). Thus, biaxial experiments using X0-specimens with loading ratios $F_1 : F_2 = 1 : -1; 1 : 0; 1 : 1$ and different rolling directions are designed to validate the proposed material model. In this work, the experiments are named based on a combination of the testing specimen and loading ratio, i.e., shear loading X0-(1/-1), one-axial tensile X0-(1/0), and biaxial tension X0-(1/1). Moreover, mean forces and relative displacements

$$F_i = \frac{F_{i.1} + F_{i.2}}{2} \quad \text{and} \quad \Delta u_{\text{ref}.i} = u_{i.1} + u_{i.2} \quad (i = 1, 2)\,, \tag{109}$$

respectively, are used in experimental and numerical analyses, as shown Fig. 3(b).

Due to its symmetry, only a quarter of the X0-specimen is used for the numerical calculations. The mesh and corresponding boundary conditions are shown in Figs. 3(c) and (d), respectively. Fine meshes are used in the notch area, as damage occurs and develops in this region, with a mesh dimension of $0.25\,\text{mm} \times 0.125\,\text{mm} \times 0.1\,\text{mm}$. It should be mentioned that the mesh size used was determined by comparing the experimentally measured strain distribution with numerical simulations. In addition, the same mesh size is also used to predict material behavior using a damage model with isotropic plasticity, as performed by Wei et al. (2023, 2024b,a). The corresponding numerical results show good agreement with the experimental ones. On the other hand, the displacement boundary condition is used in the numerical simulations. As shown in Fig. 3(c), the displacements u_1 and δu_1 are applied along axes 1 and 2, respectively. It is evident that the coefficient δ is unknown. Thus, Wei et al. (2025a) proposed an iterative approach based on analyzing the actual force ratio to update the unknown factor δ. For each loading case, the initial value of δ is assumed to be equal to the force ratio, i.e., $\delta^{\text{tr}} = \delta^{\text{exp}} = \xi$. The reaction force ratio $\delta^{\text{sim}} = F_1/F_2$ is calculated during each time step. If $\left|\delta^{\text{exp}} - \delta^{\text{sim}}\right| \leq 0.0005$, the calculation results are saved as a history variable, and the process continues to the next loading step. Otherwise, the current time step is restarted with an updated value δ^{tr}, calculated using the following equations

$$\delta^{\text{tr}} = \begin{cases} \delta^{\text{tr}} + \frac{\left|\delta^{\text{sim}} - \delta^{\text{exp}}\right|}{m} & \text{for} \quad \delta^{\text{sim}} < \delta^{\text{exp}} \\ \delta^{\text{tr}} - \frac{\left|\delta^{\text{sim}} - \delta^{\text{exp}}\right|}{m} & \text{for} \quad \delta^{\text{sim}} > \delta^{\text{exp}} \end{cases}, \tag{110}$$

where m is a numerical parameter, suggested to be 150 in the present work. As shown in the numerical results for the loading cases X0-(1/-1) and X0-(1/1) in Fig. 4, a maximum of two iterations is required to reach the designed ratios of 1:-1 and 1:1. This demonstrates the efficiency of the proposed iteration approach. Moreover, the displacement ratio used in the numerical simulation for the experiment X0-(1/-1) increases from −1 to −0.94 with increasing relative displacement Δu_{ref}, as calculated based on Eq. (109), whereas for the loading case X0-(1/1), it remains nearly constant at a value of 1. This finding highlights the symmetric property of the X0-specimen, as it generates the same force when the same displacement is applied along different axes. However, positive and negative displacements of the same magnitude induce different reaction forces, revealing a slight difference between tensile and compressive loading.

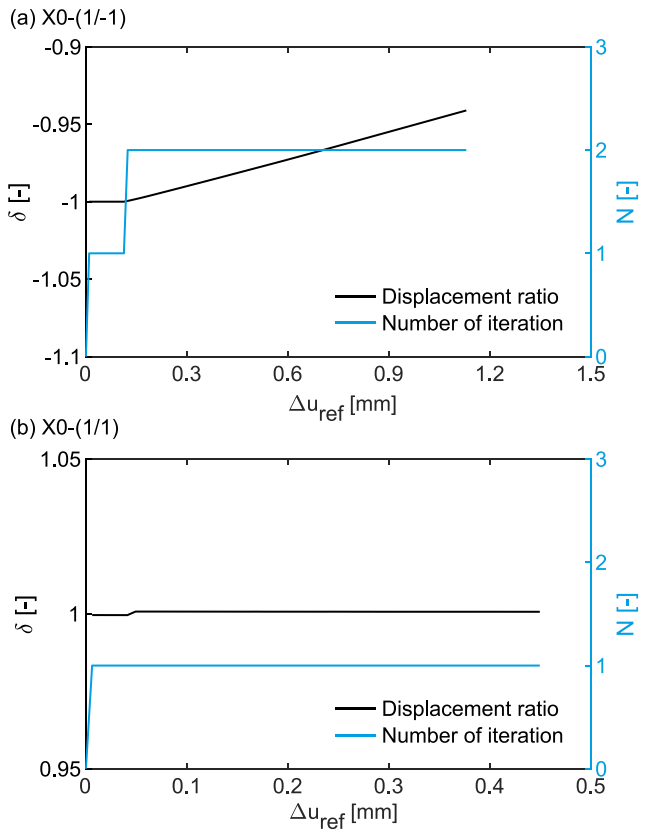

Fig. 4. Numerically predicted displacement boundary ratio δ and respective maximum iterations N.

Table 1
Chemical composition of investigated anisotropic aluminum alloy EN AW-2017A (% weight).

Al	Cu	Fe	Mn	Mg	Si	Zn	Cr	Others
to balance	4.0	0.7	0.7	0.7	0.5	0.25	0.10	0.15

6.3. Material parameters

The high-strength aluminum alloy EN AW-2017 A (EN AW-AlCu4 MgSi), which is widely used in the aerospace and automotive industries, is used to investigate anisotropic plasticity and damage properties. The chemical properties of the investigated anisotropic aluminum alloy are summarized in Table 1. The load–displacement curves differ among the rolling direction (RD), diagonal direction (DD), and transverse direction (TD). The true stress-true strain curves can be derived based on the load–displacement curves in different rolling directions. The elastic and plastic strain components can be calculated using the measured Young's modulus $E = 72000$ MPa. Then, the Lankford coefficients can be determined based on the plastic strain rate. The details of the identified r-values are discussed by Brünig et al. (2023a). With the r-values in hand, the anisotropic material parameters in Eqs. (26) and (27) can be further identified. The hardening and damage parameters are derived from the stress–strain curve for RD as a reference value. Table 2 summarizes all relevant material coefficients. The details of the identification strategy can also be found in previous publications (Brünig et al., 2023a).

7. Experimental and numerical results

The load–displacement curves for biaxial tests using X0-specimens are illustrated in Fig. 5, and a comparison of the experimental and numerical results for each loading condition and loading direction is additionally shown in Fig. B.11 in Appendix B. It is evident that the numerically predicted load–displacement curves agree well with the experimental results. In addition, the mean relative force errors R between experiments and numerical simulations are summarized in Table 3. It can be observed that most error values R are below 5%, indicating that the proposed model accurately captures the global load–displacement curve under different loading conditions and rolling directions. Moreover, the average relative errors $\bar{R} = 0.020$ for all loading cases in RD are slightly smaller than those in DD and TD, as the same hardening parameters are used in this study, which were identified based on the uniaxial tensile test for RD. On the other hand, the absolute fracture forces $\left|F^{\mathrm{fr,exp}}\right|$ and the relative fracture displacements along axis 1 ($\Delta u_1^{\mathrm{fr,exp}}$) and axis 2 ($\Delta u_2^{\mathrm{fr,exp}}$) are shown in Table 3. For all loading cases, the experimental fracture forces for DD are smaller than those for RD and TD. However, the absolute fracture displacements for loading conditions X0-(1/-1) and X0-(1/0) are greater than those for RD and TD. The material exhibits lower yield strength and slightly reduced ductility for DD compared to RD and TD. In addition, the absolute fracture displacements along axis 1 ($\Delta u_1^{\mathrm{fr,exp}}$) differ from those along axis 2 ($\Delta u_2^{\mathrm{fr,exp}}$) for experiment X0-(1/-1), with a ratio of $\Delta u_1^{\mathrm{fr,exp}}/\Delta u_2^{\mathrm{fr,exp}} = -0.83$. This value differs from the boundary displacement ratio δ, see Fig. 4(a), due to differences in relative displacements, indicating the effect of nonlinearity in the applied boundary displacement and reaction relative displacements. For the loading case X0-(1/0), the specimen is stretched along axis 1 and compressed along axis 2. It can also be observed that the fracture forces $F^{\mathrm{fr,exp}}$ in the biaxial tensile test X0-(1/1) and the one-axial tensile test X0-(1/0) are nearly the same, whereas the fracture displacements differ significantly. The above discussions highlight the influence of loading conditions and rotation on the global load–displacement curves.

Table 2
Elastic–plastic-damage material parameters.

Symbol	In Eq.	Description	Value	Unit
E		E-modulus	72 000	MPa
ν		Poisson's ratio	0.3	–
$\eta_1 ... \eta_4$	(20)	Elastic damage moduli	−10000	MPa
c_0	(30)	Initial yield stress	323	MPa
R_0	(30)	Isotropic hardening modulus	380	MPa
R_∞	(30)	Isotropic hardening modulus	122	MPa
b	(30)	Isotropic hardening exponent	16	–
C_1	(26)	Hydrostatic stress coefficient	−0.042	–
C_2	(26)	Hydrostatic stress coefficient	−0.010	–
C_3	(26)	Hydrostatic stress coefficient	0.0	–
C_4	(27)	Anisotropy parameter	0.812	–
C_5	(27)	Anisotropy parameter	1.360	–
C_6	(27)	Anisotropy parameter	1.310	–
C_7	(27)	Anisotropy parameter	3.758	–
C_8	(27)	Anisotropy parameter	3.0	–
C_9	(27)	Anisotropy parameter	3.0	–
σ_0	(41)	Initial equivalent damage stress	480	MPa
H	(41)	Isotropic softening modulus	0.05	MPa

The digital image correlation (DIC) technique is used in the experiments to record deformation and strain changes. Thus, a comparison between the experimentally measured and numerically predicted first principal strains A_1 on the notch surfaces is shown in Figs. 6(a)–(c). In addition, the mean values of the first principal strain $\bar{A}_1$ in the central region of interest (ROI) are measured by DIC and calculated in numerical simulations to quantitatively evaluate the change in the first principal strain during the loading stage, as illustrated in Figs. 6(d)–(f). It is worth noting that the maximum mean values $\bar{A}_1$ differ in Figs. 6(a)–(c), as the maximum first principal strain A_1 might not be observed at the center of the notch surface due to strain inhomogeneity. The strain paths differ significantly among different loading conditions but show only slight variations in orientations. The agreement in strain

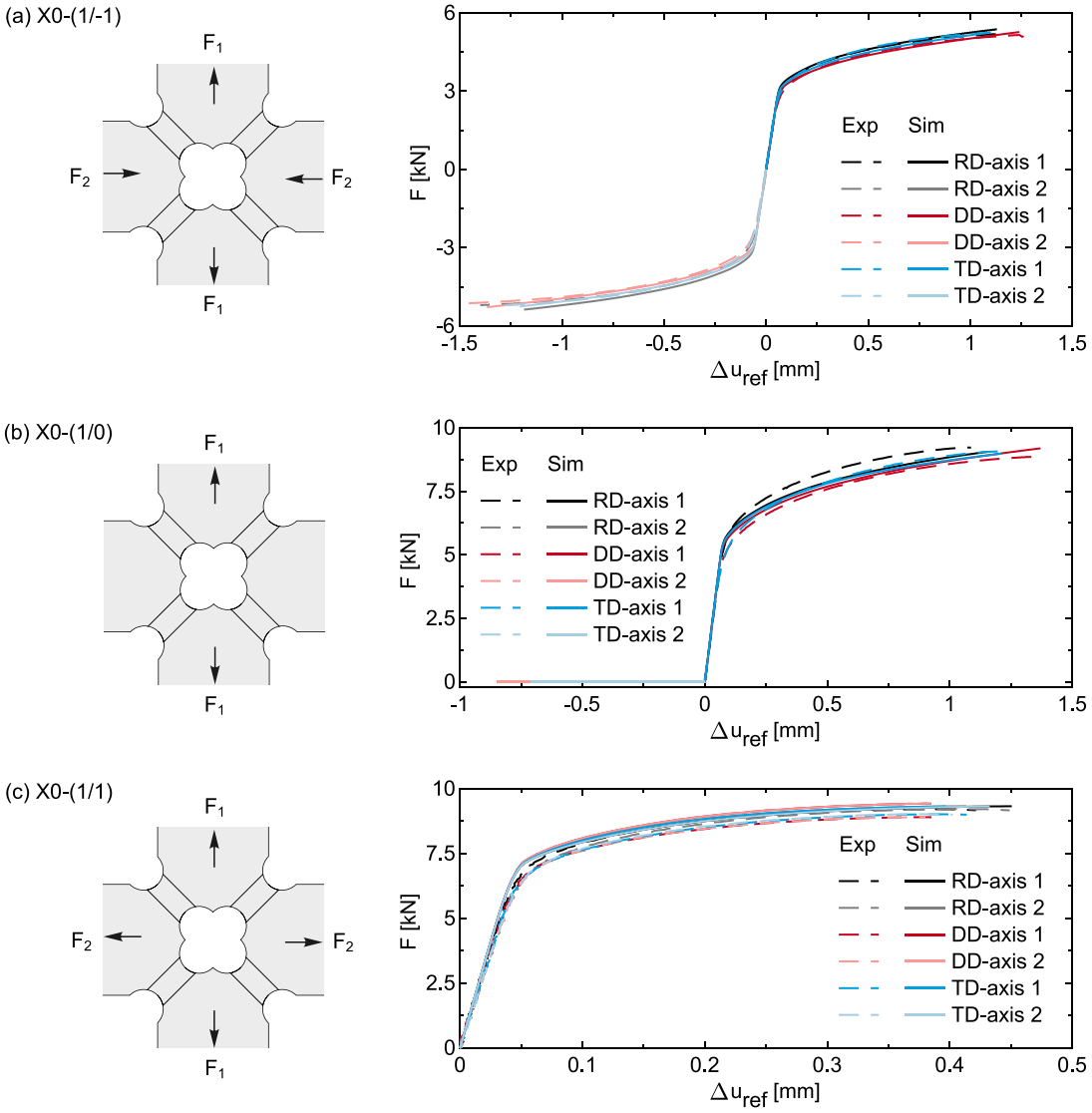

Fig. 5. Experimentally measured and numerically predicted load–displacement curves.

Table 3
Experimental fracture forces, fracture displacements, and relative errors between experiments and simulations.

	X0-(1/-1)				X0-(1/0)				X0-(1/1)				$\bar{R}$ [-]
	$\lvert F^{fr,exp}\rvert$ [kN]	$\Delta u_1^{fr,exp}$ [mm]	$\Delta u_2^{fr,exp}$ [mm]	R [-]	$\lvert F^{fr,exp}\rvert$ [kN]	$\Delta u_1^{fr,exp}$ [mm]	$\Delta u_2^{fr,exp}$ [mm]	R [-]	$\lvert F^{fr,exp}\rvert$ [kN]	$\Delta u_1^{fr,exp}$ [mm]	$\Delta u_2^{fr,exp}$ [mm]	R [-]	
RD	5.21	1.16	−1.40	0.012	9.22	1.09	−0.45	0.042	9.17	0.42	0.45	0.005	0.020
DD	5.12	1.26	−1.54	0.010	8.85	1.36	−0.58	0.017	8.90	0.39	0.38	0.057	0.028
TD	5.23	1.08	−1.32	0.024	9.06	1.21	−0.53	0.014	9.00	0.41	0.40	0.038	0.025

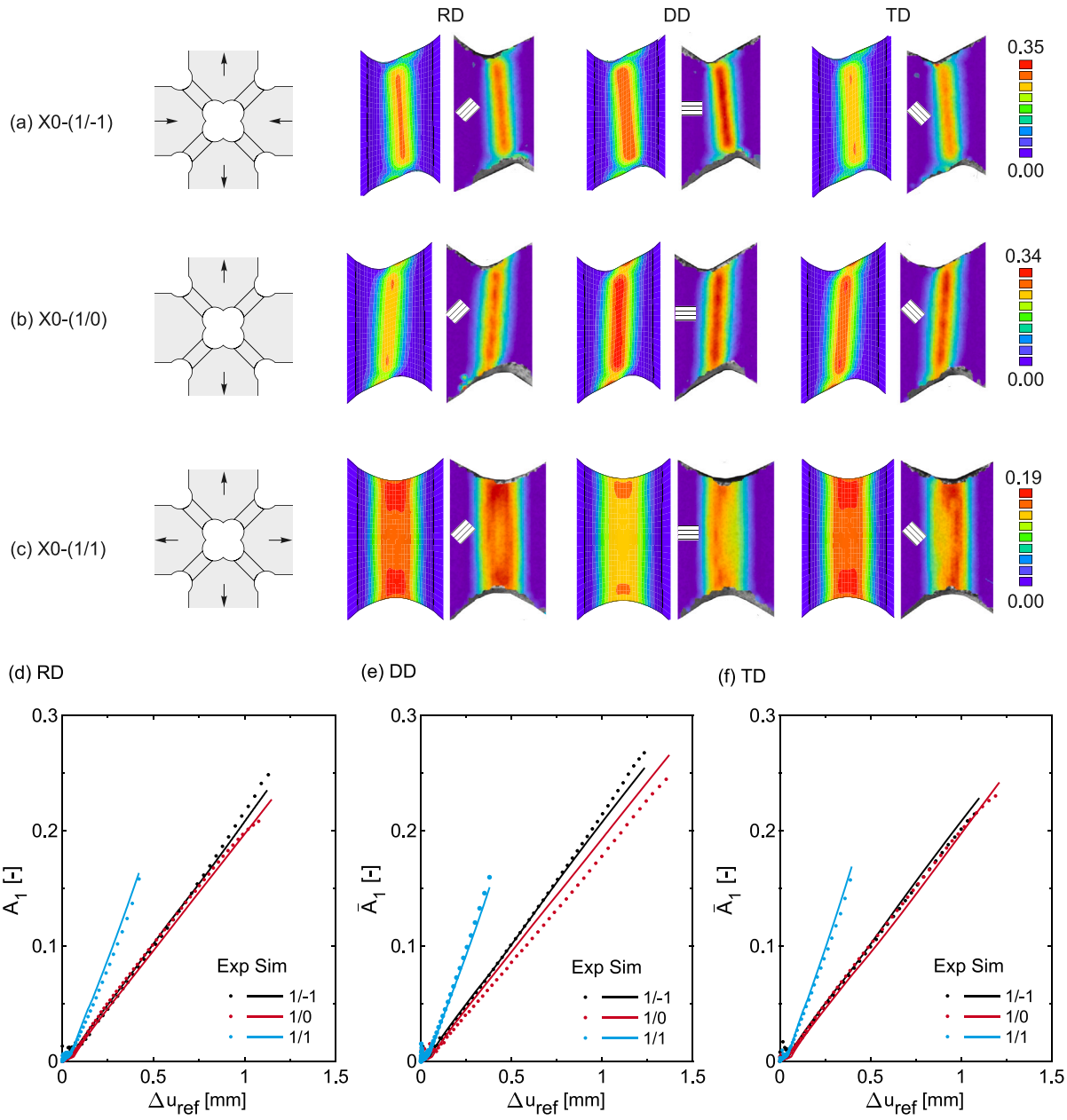

Fig. 6. Experimentally measured and numerically predicted the first principal strains A_1 on the notch surfaces just before failure (a)–(c), and experimental and numerical relative displacement Δu_{ref} versus first principal strain $\bar{A}_1$ at the regional area of the notch surface (d)–(f). The black line in the rectangular box represents the rolling direction.

distributions and strain paths between experiments and numerical calculations highlights the accuracy of the proposed material model and numerical integration method.

Different distributions of the first principal strains A_1 can be observed under various loading conditions, and all numerical results align well with the experimental ones. For the loading case X0-(1/-1), the first principal strains A_1 localized as a diagonal shear band from the top left to the bottom right. The maximum values of A_1 for the experiments in RD and TD are 0.30 and 0.28, respectively, whereas the maximum value of $A_1 = 0.35$ for DD is greater than those of RD and TD since the fracture displacement is greater than in other orientations, as shown in Table 3. Compared to the loading case X0-(1/-1), the first principal strains are also localized as a shear band but are oriented from the top right to the bottom left at an angle of about 4° with respect to the vertical axis for the experiment X0-(1/0). Again, the maximum first principal strain $A_1 = 0.34$ in loading DD is significantly greater than in loadings RD and TD. Moreover, the trend of the maximum values of the first principal strains is consistent with the fracture displacements along axis 1 ($\Delta u_1^{fr,exp}$), following the order DD>TD>RD. On the other hand, an elliptical-shaped shear band is observed and predicted for the biaxial loading condition X0-(1/1), as illustrated in Fig. 6(c). It can be observed that the maximum value of the first principal strain $A_1 = 0.15$ for the loading in DD is smaller than that of RD and TD, with a value of $A_1 = 0.19$. The analysis of experimentally measured and numerically predicted strain distributions highlights that the loading case and orientation significantly influence the local strain fields.

In the proposed material model, the damage strain tensor characterizes the deformation of micro-defects. Thus, the distributions of the accumulated equivalent damage strain μ just before failure on the notch surfaces (S) and notched cross-sections (C) are illustrated in Fig. 8. Different equivalent damage strain distributions can be observed for different loading conditions and rolling directions. In addition, since

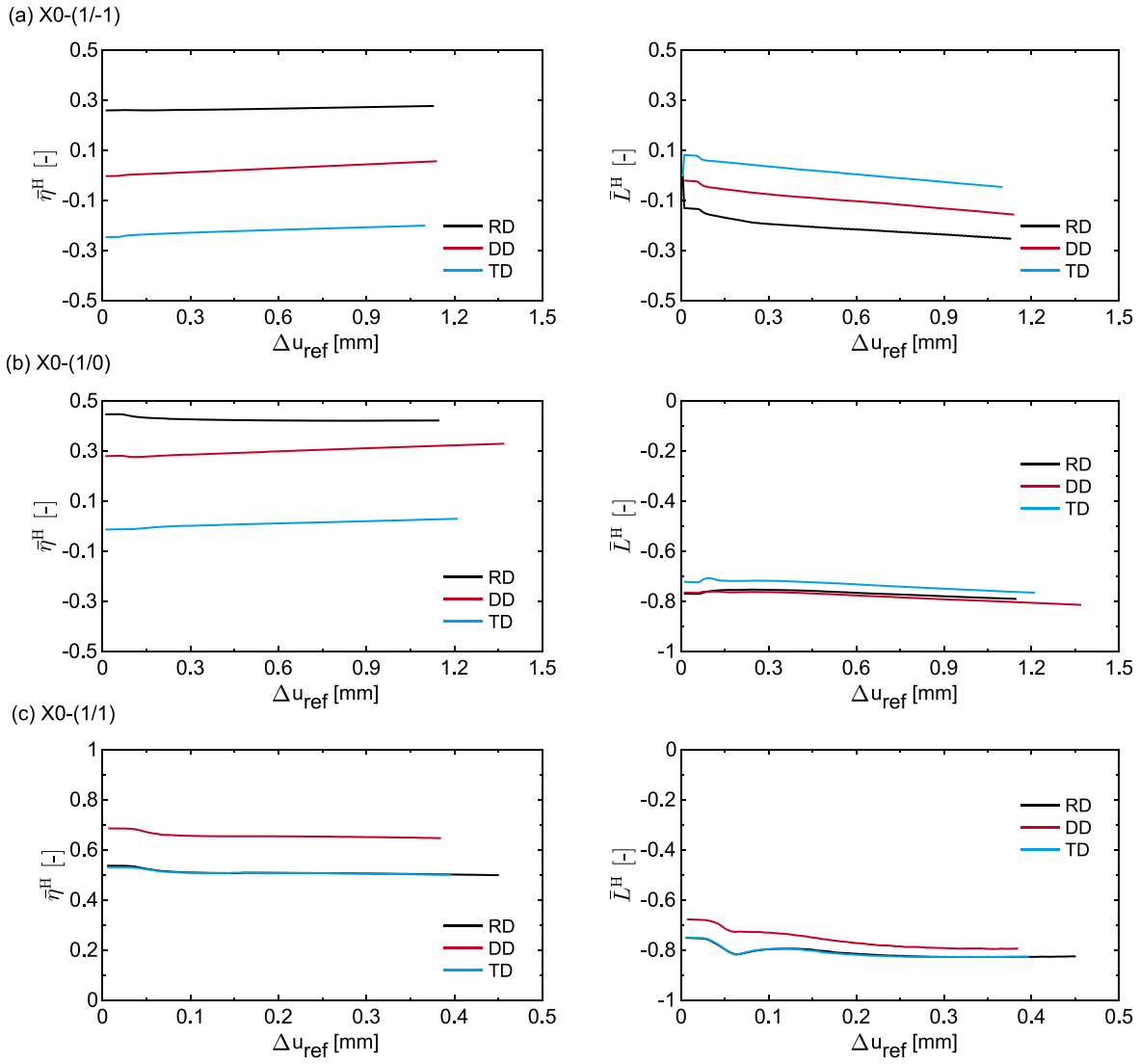

Fig. 7. The mean stress triaxiality $\bar{\eta}^{\mathrm{H}}$ and Lode parameter $\bar{L}^{\mathrm{H}}$ versus the relative displacements Δu_{ref} over the notched cross-section.

the present damage theory is stress-state-dependent, the mean stress triaxiality $\bar{\eta}^{\mathrm{H}}$ and Lode parameters $\bar{L}^{\mathrm{H}}$ over the notch cross-sections are plotted in Fig. 7. The definitions of the mean stress triaxiality $\bar{\eta}^{\mathrm{H}}$ and the Lode parameters $\bar{L}^{\mathrm{H}}$ are given by

$$\bar{\eta}^{\mathrm{H}} = \frac{1}{S}\iint_S \eta^{\mathrm{H}} ds \quad \text{and} \quad \bar{L}^{\mathrm{H}} = \frac{1}{S}\iint_S L^{\mathrm{H}} ds$$

respectively, where S denotes the total area of the notch cross-section. The mean values are introduced because the stress state variables (η^{H} and L^{H}) exhibit a nearly uniform distribution in the notch cross-section, with only a gradient at the edge of the cross-section. It can be observed that the stress triaxialities of specimens with different orientations vary, while their respective values remain nearly constant during the loading process, as shown in Fig. 7.

For loading case X0-(1/-1), the mean stress triaxialities $\bar{\eta}^{\mathrm{H}}$ and the mean Lode parameters $\bar{L}^{\mathrm{H}}$ for loadings in RD, DD, and TD are 0.26, 0.03, and −0.22, and −0.21, −0.10, and 0.0, respectively. The different stress states induced by the different orientations result in different numerical predictions for the equivalent damage strains μ, as illustrated in Fig. 8. The maximum equivalent damage strain $\mu_{\max}$ = 0.7% is predicted for X0-(1/-1) in DD at both the top and bottom of the notch surface and cross-section. For a loading ratio of 1/-1 in RD, the distribution of the equivalent damage strain is localized as a shear band on the notch surface and the edge of the notched cross-section, with a maximum value of 0.3%. Moreover, the predicted damage occurs only at the top and bottom of the notch surface and the notched cross-section, as a low negative stress triaxiality $\bar{\eta}^{\mathrm{H}} = -0.22$ is observed. On the other hand, for X0-(1/0) loading, the stress triaxialities in RD, DD, and TD are 0.42, 0.33, and 0.04, respectively, while the corresponding mean Lode parameters are −0.79, −0.82, and −0.78, see Fig. 7(b). The damage shear bands in RD and DD loading are narrower compared to those in the TD direction, with respective maximum equivalent damage strain $\mu_{\max}$ values of 0.25%, 0.31%, and 0.31%, see Fig. 8(b). Although the maximum values of the damage strains are the same in DD and TD, the damage shear band is significantly localized on the notch surface and at the edge of the notched cross-section. In the case of biaxial loading conditions X0-(1/1), the damage strain is highly localized at the center of the notched cross-sections, indicating that fracture first occurs at its center. This observation is consistent with high-stress triaxiality, which results in tension-dominated damage mechanisms, where the crack propagates from the inside to the outside. The numerically predicted stress triaxialities are 0.49, 0.65, and 0.50 for the loading in RD, DD, and TD. In addition, as depicted in Fig. 8(c), the predicted maximum values of the equivalent damage strain $\mu_{\max}$

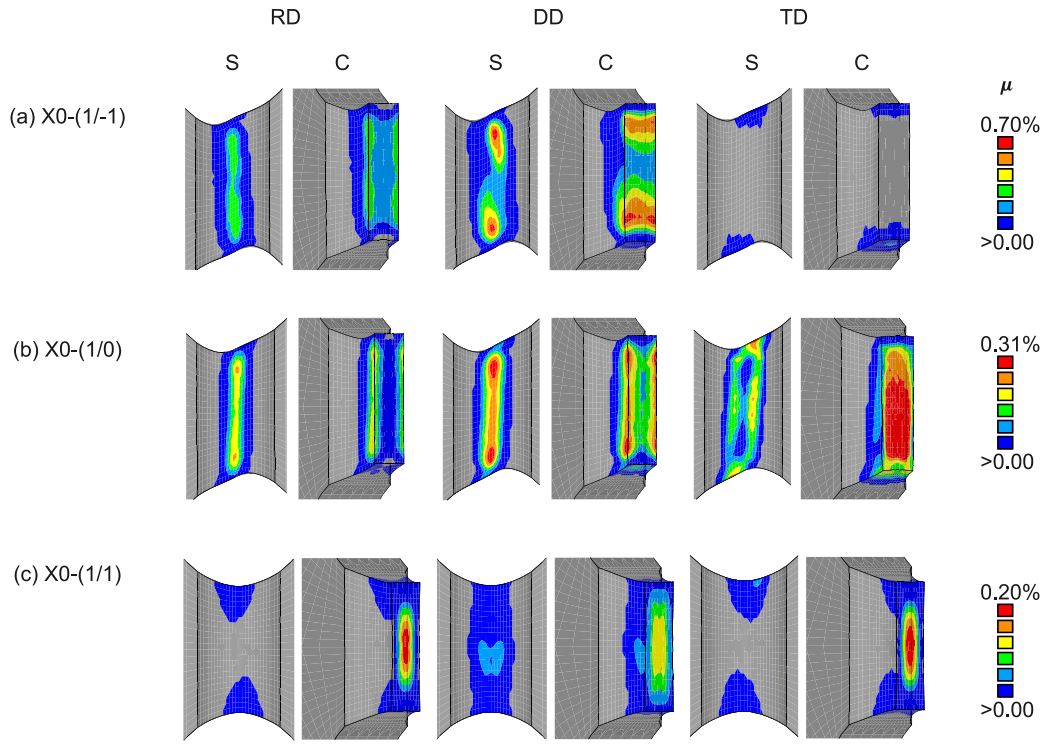

Fig. 8. Numerically predicted the equivalent damage strains μ on the notch surfaces (S) and notch cross-sections (C).

are 0.20%, 0.13%, and 0.20% for RD, DD, and TD, respectively. The above analysis of stress triaxialities and damage distributions reveals the stress-state-dependent damage mechanisms.

The damage strain evolution path for the critical element, where the maximum equivalent damage strain $\mu_{\max}$ is observed, is depicted in Fig. 9. The stress triaxiality of the critical elements for the loading condition X0-(1/-1) is 0.28, 0.09, and 0.34, respectively, with corresponding Lode parameters of −0.22, −0.21, and −0.1. The damage strain paths differ among different rolling directions, as the critical positions vary. For example, the maximum value is located on the notch surface in the DD, whereas it appears on the edge surface for TD, see Fig. 8(a). In the one-axial tension experiment X0-(1/0), the Lode parameters for all rolling directions are equal to −1 for the critical elements. However, different stress triaxialities are observed in RD, DD, and TD, with values of 0.39, 0.39, and 0.11, respectively. For the biaxial tension loading conditions X0-(1/1), the critical elements are all detected in the center of the notched cross-sections. The corresponding stress triaxialities are 0.84, 0.98, and 0.83, respectively. In addition, the stress triaxialities for the critical elements in experiments X0-(1/-1)-DD and X0-(1/0)-TD are the same, but the Lode parameters differ significantly, with values of −0.21 and −1.0, respectively. Moreover, the experiment X0-(1/-1)-TD has the same Lode parameter ($L^{\mathrm{H}} = -1$) as experiment X0-(1/0), but a smaller stress triaxiality ($\eta^{\mathrm{H}} = 0.34$) is observed. Additionally, the damage strain paths differ. These findings reveal the stress-state dependence of damage evolution and indicate that the combination of stress triaxiality and the Lode parameter plays an important role in the analysis of the stress state.

The fracture lines and fracture surfaces are shown in Fig. 10, where selected fracture surfaces are examined using the scanning electron microscopy (SEM) technique. This work uses the electron microscope EVO MA 15, manufactured by Carl Zeiss Microscopy GmbH, Germany. The obtained SEM images are used to validate the numerically predicted damage mechanisms resulting in fracture. The specimens failed at both diagonal notches in the center areas in all loading cases. The fracture lines are slightly diagonally oriented, with an angle of approximately 5° from the bottom-left to the top-right for experiment X0-(1/-1) and 7° from the top-left to the bottom-right relative to the horizontal axis for loading X0-(1/0), respectively, see Figs. 10(a) and (b). In the case of biaxial loading X0-(1/1), the fracture lines are parallel to the horizontal axis, consistent with the prediction of the first principal strains. In addition, it is worth noting that the fracture lines in Fig. 10(c) are rougher compared to those in Fig. 10(a) and (b), characteristic of the cup-cone formation observed in tension-dominated fractures. By comparing the SEM images across all loading conditions, larger deformed and coalesced micro-voids are significantly visible on the fracture surfaces under biaxial tensile loading conditions X0-(1/1), whereas only negligible micro-voids can be observed on the fracture surface in experiments X0-(1/-1). Micro-shear-cracks dominate the smooth and flat fracture surface under shear loading X0-(1/-1), resulting in a shear damage mechanism, as illustrated in Fig. 10(a). This behavior is characterized by low positive and negative stress states with low Lode parameter values, as shown in Fig. 7(a). In addition, more coalesced micro-voids and larger voids can also be observed compared to the SEM images in experiments X0-(1/0). Taking the respective stress triaxialities into account, see Figs. 7(b) and (c), it can be concluded that higher stress states induce larger micro-voids. When comparing different orientations for loading case X0-(1/1), the depth and size of micro-voids are slightly smaller in DD compared to those in RD and TD, as indicated by the numerically predicted quantitative values of the equivalent damage strain μ.

Moreover, analysis of the numerically predicted damage strain under shear loading conditions (X0-(1/-1)) shows that the damage strain components in the shear directions are significantly larger than those in the tensile (diagonal) direction, indicating that the damage is caused by the deformation of micro-shear-cracks, as illustrated in Fig. 10(a). In contrast, under tensile loading (X0-(1/0)) and biaxial loading (X0-(1/1)), the damage strain components in the diagonal directions contribute much more than those in the shear directions, confirming that the dominant mechanism is the growth of micro-voids, as illustrated in Figs. 10(b) and (c). Furthermore, the present work does not provide a detailed discussion or material modeling of fracture behavior. Following Brünig et al. (2021b), a fracture criterion based on the damage

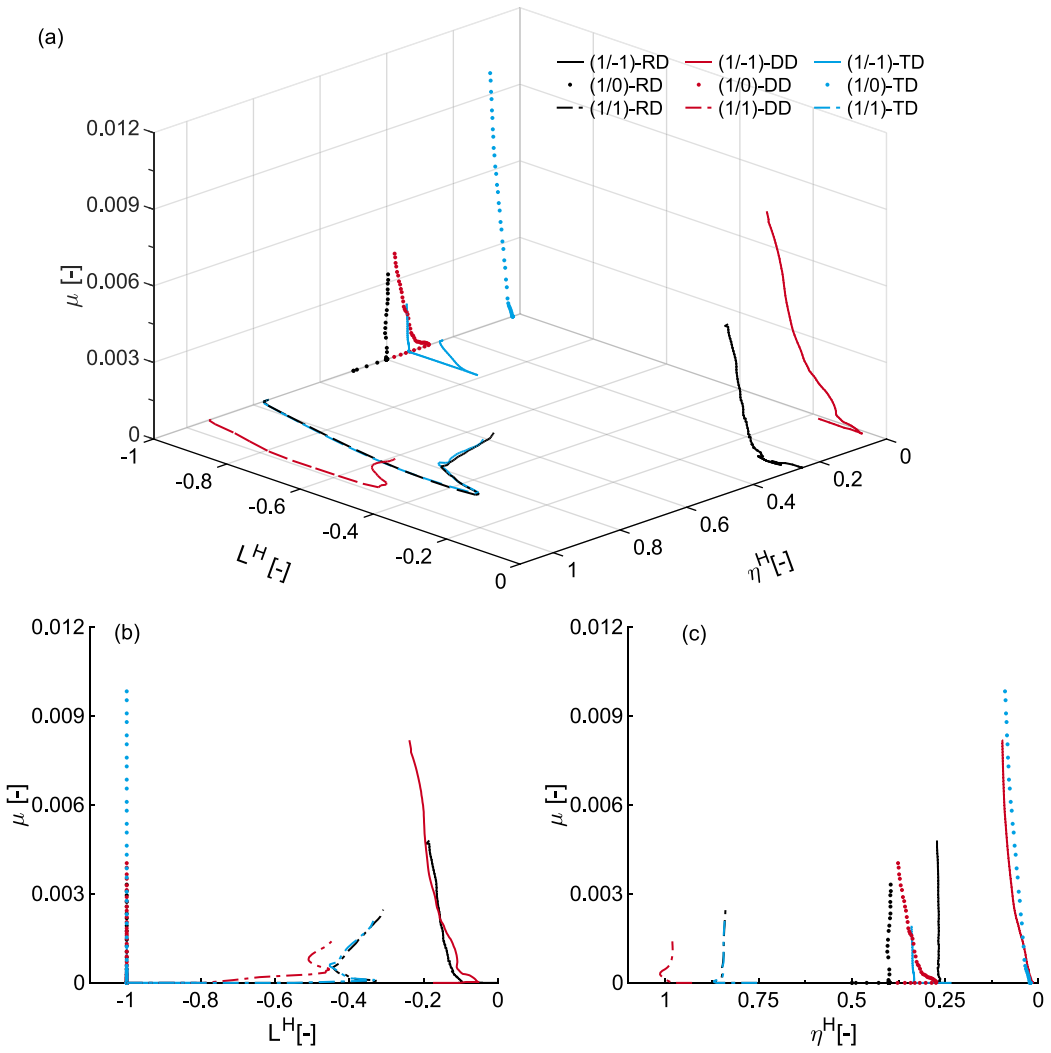

Fig. 9. Numerically predicted the equivalent damage strain μ versus the Lode parameter L^{H} and the stress triaxiality η^{H} for the critical element (a), as well as the projection of μ versus L^{H} (b) and μ versus η^{H} (c).

strain tensor has been proposed. However, it does not account for the anisotropic behavior induced by the rolling direction. For future work, a fracture criterion based on the damage strain tensor that explicitly considers the anisotropy caused by the rolling direction should be further investigated. This would allow more accurate simulations of crack path formation and provide deeper insights into how damage evolution influences the final fracture behavior, both at the micro- and macro-levels. It should also be mentioned that for more accurate simulations of significant softening due to damage and fracture behavior, the proposed local damage model may suffer from mesh sensitivity, i.e., it might be highly mesh dependent. This mesh dependency can be addressed by using the DIC-measured strain field to select an appropriate mesh size, or by applying regularization approaches (Davaze et al., 2021; Bergo et al., 2021; Yin et al., 2025; Zhang et al., 2025) such as gradient or non-local damage methods.

8. Conclusion

The anisotropic damage framework based on Brünig (2003a) has been enhanced by introducing anisotropic plasticity, which characterizes the anisotropic plastic behavior. Following the explicit inelastic predictor–elastic corrector integration approach used by Brünig (2003b) and Wei et al. (2024b), it integrates the rate equation of the newly proposed two-surface anisotropic damage model with anisotropic plasticity. The consistent tangent moduli have been derived for different states, such as pure elastic, elastic with previous damage, elastic–plastic with or without previous damage, and elastic–plastic damage. The proposed material model has been implemented in ANSYS as a user-defined subroutine.

A series of complex biaxial loading experiments with RD, DD, and TD orientations are tested to verify the proposed material model and assess the accuracy, stability, and efficiency of the numerical algorithm. Different numerical calculation results agree well with the experimental ones in various aspects, such as the global load–displacement curves with approximately 3% relative error, the distribution of local strain fields, and the evolution of strain paths during the loading process. In the numerical calculations, only very few iteration steps are necessary to achieve convergence. Micro-shear-cracks-induced damage and fracture are mainly observed in experiments with positive and negative loading in respective axes, i.e., loading ratio 1/-1. In contrast, the growth and coalescence of micro-voids, leading to damage and fracture, are observed in one-axial tension and biaxial tension experiments. The distribution of damage strains and the evolution of damage strain paths differ across various loading conditions and orientations, enabling accurate characterization of the elastic–plastic-damage material behavior. The numerical simulations enable an analysis of the respective stress

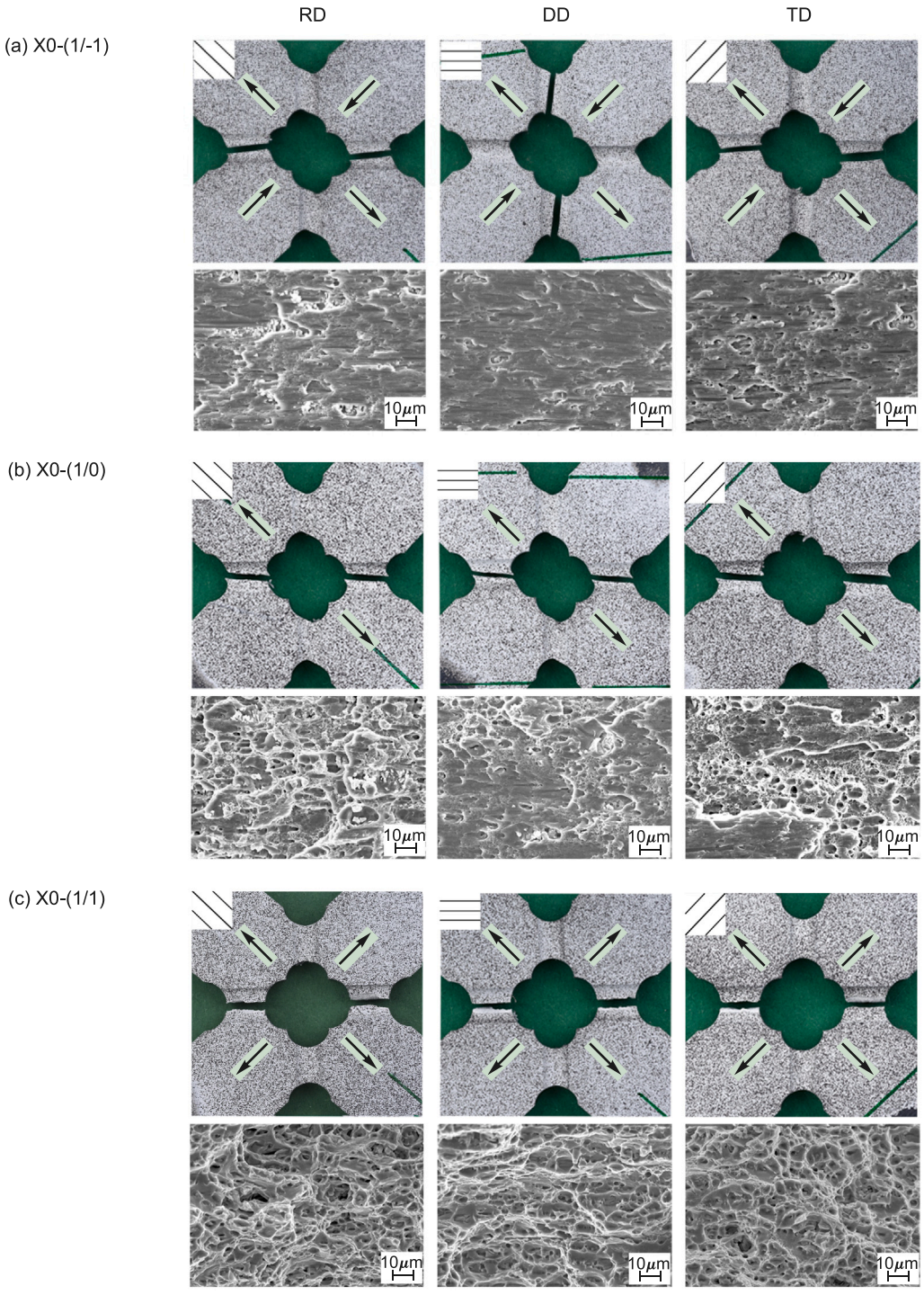

Fig. 10. Fracture lines and scanning electron microscopy (SEM) images for fracture surfaces.

states, allowing the prediction of different stress-state-dependent damage and failure modes. This is important for the estimation of the safety and lifetime of engineering structures. Most importantly, it should be noted that all numerical calculations confirm that the proposed numerical algorithm demonstrates stability and efficiency and is able to numerically simulate the experimental behavior in an accurate manner.

CRediT authorship contribution statement

Zhichao Wei: Writing – original draft, Visualization, Software, Methodology, Investigation, Formal analysis, Data curation, Conceptualization. **Sanjeev Koirala:** Writing – review & editing, Validation, Software, Methodology, Investigation, Data curation, Conceptualization. **Steffen Gerke:** Writing – review & editing, Validation, Methodology, Investigation, Conceptualization. **Michael Brünig:** Writing – review & editing, Supervision, Resources, Project administration, Methodology, Funding acquisition, Conceptualization.

Declaration of competing interest

The authors declare that they have no known competing financial interests or personal relationships that could have appeared to influence the work reported in this paper.

Acknowledgments

The project has been funded by the Deutsche Forschungsgemeinschaft (DFG, German Research Foundation), Germany – project number 394286626 (BR1793/20-1), this financial support is gratefully acknowledged. The SEM images of the fracture surfaces presented in this paper were performed at the Institut für Werkstoffe im Bauwesen, University of the Bundeswehr Munich and the support of Wolfgang Saur is gratefully acknowledged.

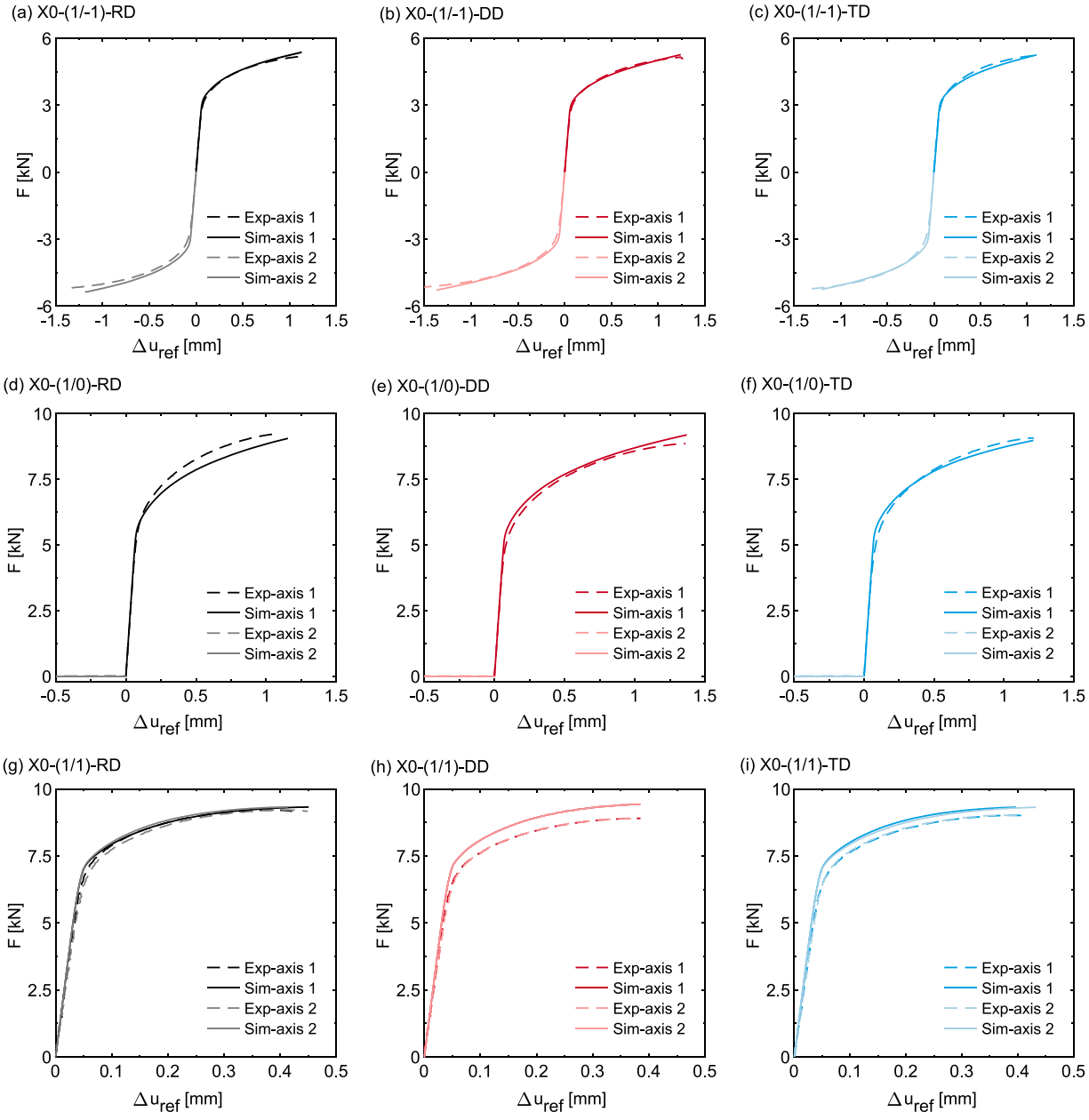

Fig. B.11. Experimental and numerical load–displacement curves for different loading conditions and rolling directions (RD, DD, and TD).

Appendix A. Definition of plastic parameters C_1-C_9

In this section, the calculation of the parameters $C_1 ... C_3$ in **C** (26) and the anisotropic tensor $\mathbb{D}$ (27) is presented as follows. For more details of the identification procedure, see Brünig et al. (2023a). The effective stresses are defined as follows: $\bar{T}_{Tx}$ and $\bar{T}_{Cx}$ denote the stresses obtained from tension and compression tests, respectively, with specimens cut in the RD (x-direction), whereas $\bar{T}_{Ty}$ and $\bar{T}_{Cy}$ denote the corresponding stresses from specimens cut in the TD (y-direction). S_{xy} means the yield stress of the shear test. In addition, the Lankford coefficient can be calculated as

$$r_\theta = \frac{-\dot{H}^{pl}_{\theta+90°}}{\dot{H}^{pl}_x + \dot{H}^{pl}_y} \tag{A.1}$$

where θ denotes the angle relative to the rolling direction, see Brünig et al. (2021a).

$$C_1 = \frac{1}{2}\left(1 - \frac{\bar{T}_{Tx}}{\bar{T}_{Cx}}\right), \quad \text{and} \quad C_2 = \frac{1}{2}\bar{T}_{Tx}\left(\frac{1}{\bar{T}_{Ty}} - \frac{1}{\bar{T}_{Cy}}\right) \tag{A.2}$$

$$C_5 = \frac{1}{2\left(1+r_0\right)}\left(1 + \frac{\bar{T}_{Tx}}{\bar{T}_{Cx}}\right)^2, \quad \text{and} \quad C_4 = r_0\, C_5 = \frac{1}{2}\left(1 + \frac{\bar{T}_{Tx}}{\bar{T}_{Cx}}\right)^2 - C_5 \tag{A.3}$$

$$C_6 = \frac{C_4}{r_{90}}, \quad \text{or} \quad C_6 = \frac{1}{2}\bar{T}^2_{Tx}\left(\frac{1}{\bar{T}_{Ty}} + \frac{1}{\bar{T}_{Cy}}\right)^2 - C_4 \tag{A.4}$$

$$C_7 = \left(r_{45} + \frac{1}{2}\right)(C_5 + C_6), \quad \text{or} \quad C_7 = \frac{1}{\bar{T}^2_{Sxy}}\left[\left(\bar{T}_{Tx} - C_1\bar{T}_{Tx}\right)^2 - \frac{1}{2}(C_4 + C_5)\bar{T}^2_{Tx}\right] \tag{A.5}$$

Appendix B. Load–displacement curves for different loading conditions and rolling directions

See Fig. B.11.

Data availability

Data will be made available on request.

References

Abu Al-Rub, R.K., Voyiadjis, G.Z., 2003. On the coupling of anisotropic damage and plasticity models for ductile materials. Int. J. Solids Struct. 40, 2611–2643.

Alzweighi, M., Mansour, R., Tryding, J., Kulachenko, A., 2022. Evaluation of Hoffman and xia plasticity models against bi-axial tension experiments of planar fiber network materials. Int. J. Solids Struct. 238, 111358.

Anand, L., 1979. On H. Hencky's approximate strain-energy function for moderate deformations. J. Appl. Mech 46, 78–82.

Badreddine, H., Saanouni, K., 2017. On the full coupling of plastic anisotropy and anisotropic ductile damage under finite strains. Int. J. Damage Mech. 26, 1080–1123.

Bai, Y., Wierzbicki, T., 2008. A new model of metal plasticity and fracture with pressure and Lode dependence. Int. J. Plast. 24, 1071–1096.

Barlat, F., Aretz, H., Yoon, J.W., Karabin, M.E., Brem, J.C., Dick, R.E., 2005. Linear transfomation-based anisotropic yield functions. Int. J. Plast. 21, 1009–1039.

Bergo, S., Morin, D., Sture Hopperstad, O., 2021. Numerical implementation of a non-local GTN model for explicit FE simulation of ductile damage and fracture. Int. J. Solids Struct. 219–220, 134–150.

Brünig, M., 1999. Large strain elastic–plastic theory and nonlinear finite element analysis based on metric transformation tensors. Comput. Mech. 24, 187–196.

Brünig, M., 2001. A framework for large strain elastic–plastic damage mechanics based on metric transformations. Internat. J. Engrg. Sci. 39, 1033–1056.

Brünig, M., 2003a. An anisotropic ductile damage model based on irreversible thermodynamics. Int. J. Plast. 19, 1679–1713.

Brünig, M., 2003b. Numerical analysis of anisotropic ductile continuum damage. Comput. Methods Appl. Mech. Engrg. 192, 2949–2976.

Brünig, M., Chyra, O., Albrecht, D., Driemeier, L., Alves, M., 2008. A ductile damage criterion at various stress triaxialities. Int. J. Plast. 24, 1731–1755.

Brünig, M., Gerke, S., Koirala, S., 2021a. Biaxial experiments and numerical analysis on stress-state-dependent damage and failure behavior of the anisotropic aluminum alloy EN AW-2017A. Metals 11 (1214).

Brünig, M., Koirala, S., Gerke, S., 2022. Analysis of damage and failure in anisotropic ductile metals based on biaxial experiments with the H-specimen. Exp. Mech. 62, 183–197.

Brünig, M., Koirala, S., Gerke, S., 2023a. A stress-state-dependent damage criterion for metals with plastic anisotropy. Int. J. Damage Mech. 32, 811–832.

Brünig, M., Koirala, S., Gerke, S., 2023b. Micro-mechanical numerical analysis on ductile damage in multiaxially loaded anisotropic metals. Comput. Mech. 73, 223–232.

Brünig, M., Schmidt, M., Gerke, S., 2021b. A fracture criterion for ductile metals based on critical damage parameters. Contin. Mech. Thermodyn. 101, 1–1022.

Costin, L.S., 1985. Damage mechanics in the post-failure regime. Mech. Mater. 4, 149–160.

Davaze, V., Vallino, N., Langrand, B., Besson, J., Feld-Payet, S., 2021. A non-local damage approach compatible with dynamic explicit simulations and parallel computing. Int. J. Solids Struct. 228, 110999.

Drucker, D.C., Prager, W., 1952. Soil mechanics and plastic analysis or limit design. Quart. Appl. Math. 10, 157–165.

Gao, X., Zhang, G., Roe, C., 2010. A study on the effect of the stress state on ductile fracture. Int. J. Damage Mech. 19, 75–94.

Gerke, S., Adulyasak, P., Brünig, M., 2017. New biaxially loaded specimens for the analysis of damage and fracture in sheet metals. Int. J. Solids Struct. 110–111, 209–218.

Gerke, S., Wei, Z., Brünig, M., 2024. Experiments on low-cycle ductile damage and failure under biaxial loading conditions. Exp. Mech. 64, 1021–1036.

Ha, J., Baral, M., Korkolis, Y.P., 2018. Plastic anisotropy and ductile fracture of bake-hardened AA6013 aluminum sheet. Int. J. Solids Struct. 155, 123–139.

Hayakawa, K., Murakami, S., Liu, Y., 1998. An irreversible thermodynamics theory for elastic–plastic-damage materials. Eur. J. Mech. A Solids 17, 13–32.

Hill, R., 1948. A theory of the yielding and plastic flow of anisotropic metals. Proc. R. Soc. Lond. A 193, 281–297.

Hoffman, O., 1967. The brittle strength of orthotropic materials. J. Compos. Mater. 1, 200–206.

Holmen, J.K., Frodal, B.H., Hopperstad, O.S., Børvik, T., 2017. Strength differential effect in age hardened aluminum alloys. Int. J. Plast. 99, 144–161.

Lehmann, T., 1989. Some thermodynamical considerations on inelastic deformations including damage processes. Acta Mech. 79, 1–24.

Lehmann, T., 1991. Thermodynamical foundations of large inelastic deformations of solid bodies including damage. Int. J. Plast. 7, 79–98.

Lemaitre, J., 1985. A continuous damage mechanics model for ductile fracture. J. Eng. Mater. Technol 107, 83–89.

Li, C., Fang, J., Wu, C., Sun, G., Steven, G., Li, Q., 2022. Phase field fracture in elasto-plastic solids: Incorporating phenomenological failure criteria for ductile materials. Comput. Methods Appl. Mech. Engrg. 391, 114580.

Lian, J., Sharaf, M., Archie, F., Münstermann, S., 2013. A hybrid approach for modelling of plasticity and failure behaviour of advanced high-strength steel sheets. Int. J. Damage Mech. 22, 188–218.

Lu, T.J., Chow, C.L., 1990. On constitutive equations of inelastic solids with anisotropic damage. Theor. Appl. Fract. Mech. 14, 187–218.

Mohr, D., Marcadet, S.J., 2015. Micromechanically-motivated phenomenological Hosford–Coulomb model for predicting ductile fracture initiation at low stress triaxialities. Int. J. Solids Struct. 67–68, 40–55.

Murakami, S., 1988. Mechanical modeling of material damage. J. Appl. Mech 55, 280–286.

Murakami, S., 2012. Continuum Damage Mechanics, vol. 185, Springer Netherlands, Dordrecht.

Nahshon, K., Hutchinson, J.W., 2008. Modification of the Gurson model for shear failure. Eur. J. Mech. A Solids 27, 1–17.

Nemat-Nasser, S., 1991. Rate-independent finite-deformation elastoplasticity: a new explicit constitutive algorithm. Mech. Mater. 11, 235–249.

Nemat-Nasser, S., Chung, D.T., 1992. An explicit constitutive algorithm for large-strain, large-strain-rate elastic-viscoplasticity. Comput. Methods Appl. Mech. Eng. 95, 205–219.

Nemat-Nasser, S., Li, Y.F., 1992. A new explicit algorithm for finite-deformation elastoplasticity and elastoviscoplasticity: Performance evaluation. Comput. Struct. 44, 937–963.

Nemat-Nasser, S., Li, Y.F., 1994. An algorithm for large-scale computational finite-deformation plasticity. Mech. Mater. 18, 231–264.

Ortiz, M., Popov, E.P., 1985. Accuracy and stability of integration algorithms for elastoplastic constitutive relations. Internat. J. Numer. Methods Engrg. 21, 1561–1576.

Papasidero, J., Doquet, V., Mohr, D., 2015. Ductile fracture of aluminum 2024-T351 under proportional and non-proportional multi-axial loading: Bao–Wierzbicki results revisited. Int. J. Solids Struct. 69–70, 459–474.

Park, N., Stoughton, T.B., Yoon, J.W., 2019. A criterion for general description of anisotropic hardening considering strength differential effect with non-associated flow rule. Int. J. Plast. 121, 76–100.

Roth, C.C., Mohr, D., 2016. Ductile fracture experiments with locally proportional loading histories. Int. J. Plast. 79, 328–354.
Saanouni, K., 2008. On the numerical prediction of the ductile fracture in metal forming. Eng. Fract. Mech. 75, 3545–3559.
Simo, J.C., Hughes, T.J., 1998. Computational Inelasticity, vol. 7, Springer-Verlag, New York.
Spitzig, W.A., Richmond, O., 1984. The effect of pressure on the flow stress of metals. Acta Metall. 32, 457–463.
Stoughton, T.B., Yoon, J.W., 2009. Anisotropic hardening and non-associated flow in proportional loading of sheet metals. Int. J. Plast. 25, 1777–1817.
Suaris, W., Shah, S.P., 1984. Rate–sensitive damage theory for brittle solids. J. Eng. Mech. 110, 985–997.
Tvergaard, V., Needleman, A., 1984. Analysis of the cup-cone fracture in a round tensile bar. Acta Metall. 32, 157–169.
Voyiadjis, G.Z., Hoseini, S.H., Farrahi, G.H., 2013. A plasticity model for metals with dependency on all the stress invariants. J. Eng. Mater. Technol. 135, 011002.
Voyiadjis, G.Z., Kattan, P.I., 1992. A plasticity-damage theory for large deformation of solids—I. Theoretical formulation. Int. J. Eng. Sci. 30, 1089–1108.
Wang, L.H., Atluri, S.N., 1994. An analysis of an explicit algorithm and the radial return algorithm, and a proposed modification, in finite plasticity. Comput. Mech. 13, 380–389.
Wei, Z., Gerke, S., Brünig, M., 2023. Damage and fracture behavior under non-proportional biaxial reverse loading in ductile metals: Experiments and material modeling. Int. J. Plast. 171, 103774.
Wei, Z., Gerke, S., Brünig, M., 2024a. Ductile damage and fracture characterizations in bi-cyclic biaxial experiments. Int. J. Mech. Sci. 276, 109380.
Wei, Z., Gerke, S., Brünig, M., 2024b. Numerical analysis of non-proportional biaxial reverse experiments with a two-surface anisotropic cyclic plasticity-damage approach. Comput. Methods Appl. Mech. Engrg. 419, 116630.
Wei, Z., Harting, M., Gerke, S., Brünig, M., 2025a. Ductile damage analysis under extreme low-cycle biaxial shear loadings: Experiments and simulations. Int. J. Solids Struct. 313, 113292.
Wei, Z., Mao, G., Gerke, S., Münstermann, S., Brünig, M., 2025b. Experimental analysis and modeling of anisotropic ductile damage in non-proportional extreme low-cycle biaxial loading with shear-tension histories. Int. J. Plast. 194, 104474.
Wei, Z., Zistl, M., Gerke, S., Brünig, M., 2022. Analysis of ductile damage and fracture under reverse loading. Int. J. Mech. Sci. 228, 107476.
Wu, H., Zhuang, X., Zhao, Z., 2022. Extended GTN model for predicting ductile fracture under a broad range of stress states. Int. J. Solids Struct. 239–240, 111452.
Yin, Y., Yu, H., Yan, H., Zhu, S., 2025. Diffusive-length-scale adjustable phase field fracture model for large/small structures. Int. J. Mech. Sci. 285, 109839.
Zeng, C., Fang, X., 2025. A new yield surface model considering non-uniform strain rate hardening behavior. Int. J. Mech. Sci. 301, 110504.
Zhang, Q., Ritzert, S., Zhang, J., Kehls, J., Reese, S., Brepols, T., 2025. A multi-field decomposed model order reduction approach for thermo-mechanically coupled gradient-extended damage simulations. Comput. Methods Appl. Mech. Engrg. 434, 117535.